Development of Computational Tools for Predicting the Radar Scattering from Targets on a Rough Sea Surface

R.J. Burkholder, P. Janpugdee, and D. Çolak

The Ohio State University

ElectroScience Laboratory

Department of Electrical Engineering
1320 Kinnear Road
Columbus, Ohio 43212

Final Report 735231-3
Grant No. N00014-98-1-0243
January 2001

Office of Naval Research
Program Officer: Ronald P. Radlinski
Ballston Centre Tower One
800 N. Quincy Street
Arlington, VA 22217-5660

NOTICES

When Government drawings, specifications, or other data are used for any purpose other than in connection with a definitely related Government procurement operation, the United States Government there incurs no responsibility nor any obligation whatsoever, and the fact that the Government may have formulated, furnished, or in any way supplied the said drawings. specifications, or other data, it not to be regarded by implication or otherwise as in any manner licensing the holder or any other person or corporation, or conveying any rights or permission to manufacture, use, or sell any patented invention that may in any way be related thereto.

Development of Computational Tools for Predicting the Radar Scattering from Targets on a Rough Sea Surface

R.J. Burkholder, P. Janpugdee, and D. Çolak

Final Report 735231-3
Grant No. N00014-98-1-0243
January 2001

Office of Naval Research
Program Officer: Ronald P. Radlinski
Ballston Centre Tower One
800 N. Quincy Street
Arlington, VA 22217-5660

REPORT DOCUMENTATION PAGE

Form Approved
OMB No. 0704-0188

1. AGENCY USE ONLY *(Leave blank)*	2. REPORT DATE	3. REPORT TYPE AND DATES COVERED
	January 2001	Final Report

4. TITLE AND SUBTITLE
Development of Computational Tools for Predicting the Radar Scattering from Targets on a Rough Sea Surface

5. FUNDING NUMBERS
N00014-98-1-0243

6. AUTHOR(S)
R.J. Burkholder, P. Janpugdee and D. Colak

7. PERFORMING ORGANIZATION NAME(S) AND ADDRESS(ES)
The Ohio State University
ElectroScience Laboratory
1320 Kinnear Road
Columbus, Ohio 43212

8. PERFORMING ORGANIZATION REPORT NUMBER
735231-3

9. SPONSORING/MONITORING AGENCY NAME(S) AND ADDRESS(ES)
Office of Naval Research
Ballston Centre Tower One
800 N. Quincy Street
Arlington, VA 22217-5660

10. SPONSORING/MONITORING AGENCY REPORT NUMBER

11. SUPPLEMENTARY NOTES

12a. DISTRIBUTION AVAILABILITY STATEMENT
A. Approved for public release;
Distribution is unlimited.

12b. DISTRIBUTION CODE

13. ABSTRACT *(Maximum 200 words)*

The radar scattering from 2D and 3D targets on a rough sea surface is investigated using computational techniques developed specifically for this problem. Numerical simulations and Monte Carlo studies yield insight into the scat. phenomenology. It is found that the scattering from a target on a random rough sea surface becomes more coherent as the incident field becomes more coherent, ie, for low wind speeds or low elevation angles. For the less coherent case, the avg. and peak scattering levels of a target on a rough surface may be significantly higher or lower than for a flat surface, depending on the target geometry. A tilted plane model is proposed for predicting the variations in the RCS of a target on a rough sea surface by mounting the target on a locally planar surface which can tilt, similar to the two-scale composite model of ocean scattering. It is found that tilting the plane, or equiv., rolling the target on a horiz. plane fields as much or more variation in the RCS than caused by the rough surface. However, the cross-polarization introduced by the rough surface in 3D is not well predicted by the tilted plane model, nor is the unexplained behavior near the Brewster angle for vertical polarization.

14. SUBJECT TERMS	15. NUMBER OF PAGES
	87
	16. PRICE CODE

17. SECURITY CLASSIFICATION OF REPORT	18. SECURITY CLASSIFICATION OF THIS PAGE	19. SECURITY CLASSIFICATION OF ABSTRACT	20. LIMITATION OF ABSTRACT
U	U	U	U

Acknowledgments

The authors would like to express gratitude to Dr. Marcos Rodriguez Pino and Prof. Fernando Obelleiro of the University of Vigo, Spain, for generating the Monte Carlo results for 2D targets, Dr. Dilek Colak for supplying the code for generating 3D rough surfaces, and Prof. Joel T. Johnson for contributing his expertise for modeling and analyzing rough sea surfaces.

This material is based upon work supported by the Office of Naval Research under Award No. N00014-98-1-0243,

Any Opinions, findings, and conclusions or recommendations expressed in this publication are those of the author(s) and do not necessarily reflector the views of the Office of Naval Research.

Contents

List of Figures

Chapter 1

Introduction

1.1 Background

The purpose of the research work reported here is to be able to predict and study the radar cross section (RCS) of targets on a rough sea surface using computational electromagnetics (CEM) techniques. Figure 1.1 shows a typical situation where a ship is illuminated by an incident electromagnetic (EM) plane wave, and scatters energy in all directions. It is known that the prevailing sea state (surface roughness) can greatly affect the radar scattering of a ship. The time-changing sea surface may increase or decrease the amount of energy backscattered to the receiver compared to a calm surface, so the RCS likewise changes with time. To predict the effect of the sea surface on the RCS, it is necessary to study how the incident field scatters from the rough sea surface before hitting the ship, and how the subsequent scattering from the ship interacts with the sea surface before propagating back

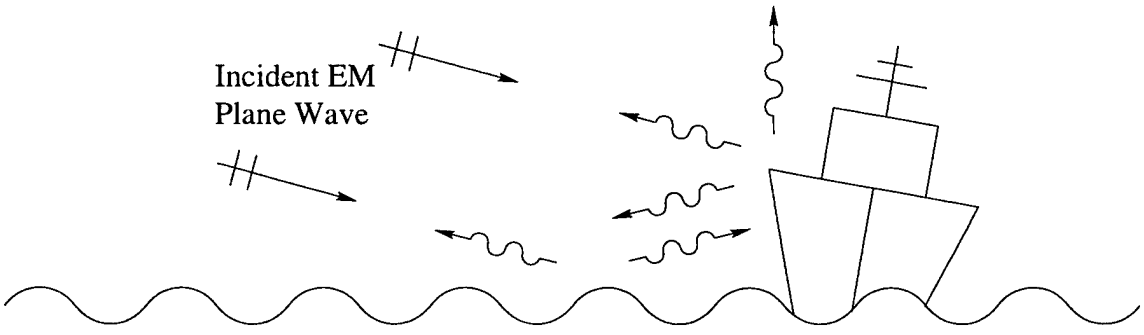

Figure 1.1: Scattering by a ship on a rough sea surface illuminated by an incident EM plane wave.

to the receiver.

This report describes the research performed during the third year of Grant No. N00014-98-1-0243 from the Office of Naval Research. The particular focus is to develop algorithms wherein existing CEM tools for predicting the RCS of a target can be modified to account for the presence of the rough sea surface, without having to include the extremely large rough surface in the computational domain. The first year's study was devoted to a thorough analysis in two dimensions (2D) of the phenomenology associated with the target/rough surface scattering problem [1]. Basic algorithms were developed and tested to provide proofs-of-concept before proceeding to more complex 3D problems. During the second year the 2D investigation was wrapped-up and the study of 3D problems was initiated [2]. The third and final year is focused primarily on studying the scattering from 3D targets, and the incident field over a spherical earth. It is shown that the conclusions reached from the 2D study extend nicely to 3D, and some new observations unique to 3D are encountered.

It is noted that the backscatter from the sea surface itself (i.e., "sea clutter") is not of interest here, but has been studied extensively [3, 4]. It is also noted that plane wave incidence is of primary interest here because the definition of RCS assumes that the source is at infinity. For typical surface-to-surface and air-to-surface radar search scenarios, this assumption implies that the downward propagating incident field is locally planar in the vicinity of the target (but the incident field reflected from the sea surface is *not* assumed to be locally planar). The propagation of the EM field from the source to the target, as well as the source and receiver gain, is not included in the plane wave RCS but is included elsewhere in the standard radar equation [4]. The power received by a radar antenna with effective aperture A_e due to scattering from a target with RCS σ is given by

$$P_r \;=\; P_t\, G\, A_e\, S^2\, \sigma \tag{1.1}$$

where P_t and G are the power and gain of the transmitting antenna, and S is the one-way propagation loss factor. For free space S is $1/4\pi R^2$, where R is the range to the target. For propagation over the sea surface, S is a much more complicated function of distance and is not the subject of this report (although results are presented in Chapter 4 for studying the

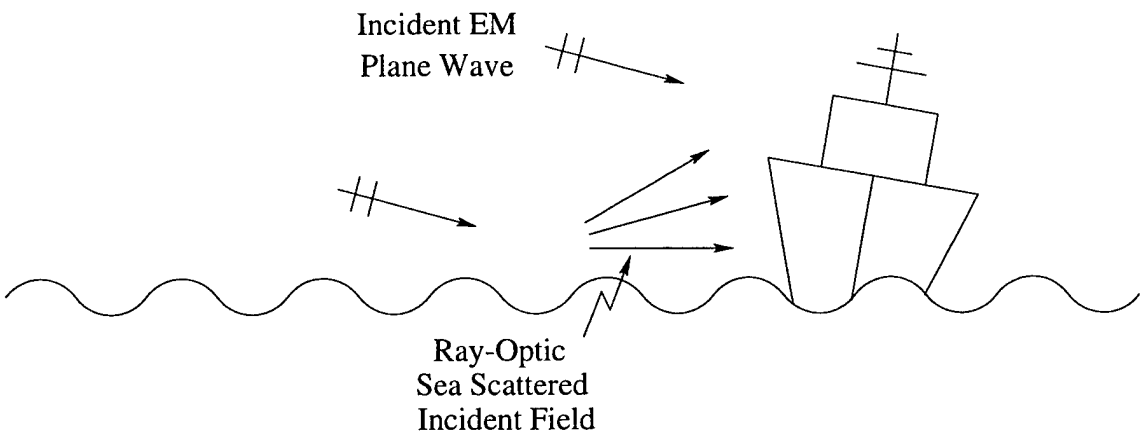

Figure 1.2: Ray-optical characterization of the field illuminating the ship.

effects of rough surfaces and a curved earth on the incident field which reaches the target).

1.2 Review of First and Second Years

Since most existing CEM tools for RCS prediction rely on a ray-optical incident field, it is of primary importance to be able to characterize the sea scattered field which illuminates the ship ray-optically, as shown in Figure 1.2. This is especially important for RCS tools which use high-frequency asymptotic methods, such as physical optics (PO), the physical theory of diffraction (PTD), and the uniform theory of diffraction (UTD) [5]. These methods must have a well-defined ray-optical incident field. Furthermore, most ship geometries are very large in terms of the wavelength of the EM field at radar frequencies, so high-frequency methods must usually be used instead of numerical methods which are better suited for smaller problems.

A discrete plane wave expansion was investigated for the ray-optical characterization of the sea scattered incident field in [1], as shown in Figure 1.3. Once the incident field is characterized ray-optically, the scattering from the ship is found approximately by replacing the rough sea surface with a locally planar surface, as shown in Figure 1.4. This allows the half-space Green's function to be used to compute the scattered field, or equivalently, image theory could be used [6]. (Although image theory is not recommended because including the image of the ship doubles the size of the problem.) The ray-optical expansion of the incident

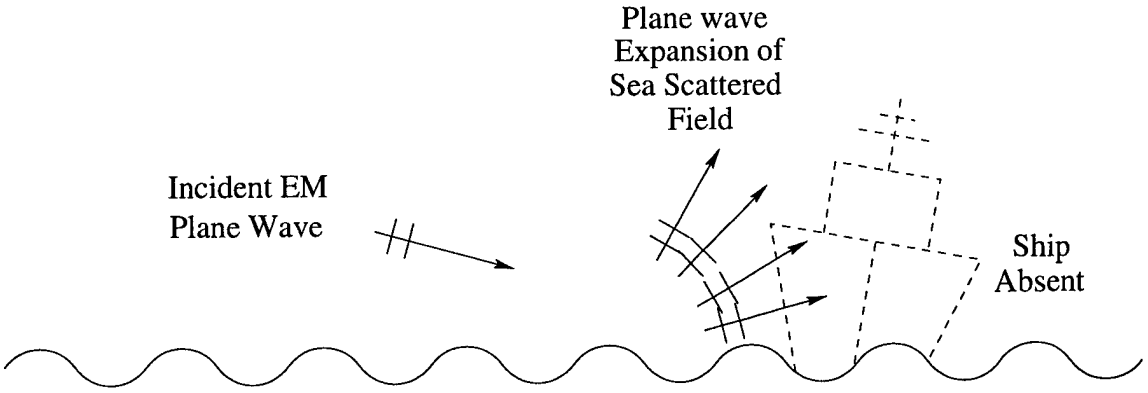

Figure 1.3: Plane wave expansion for the incident and sea scattered field illuminating the ship.

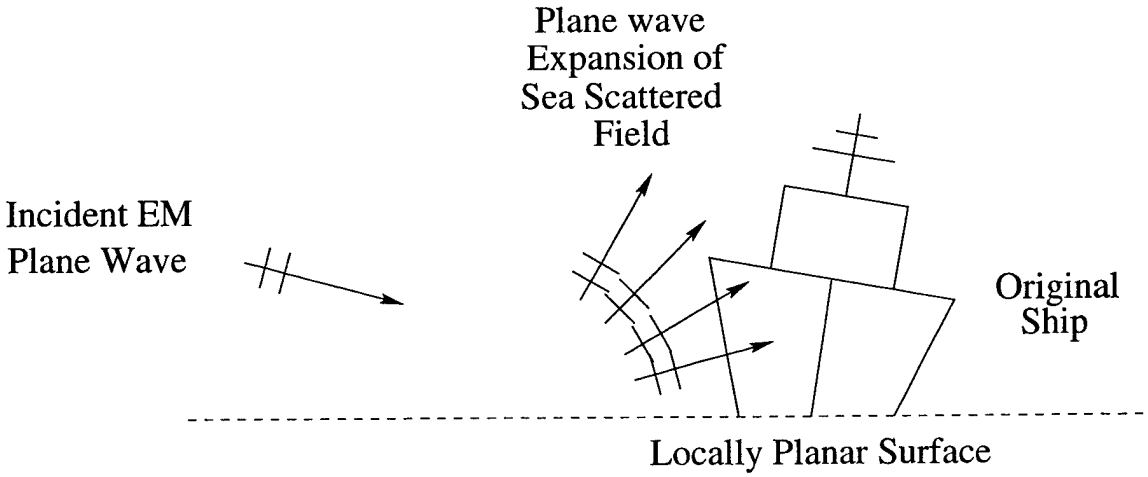

Figure 1.4: Rough sea surface replaced with a locally flat surface.

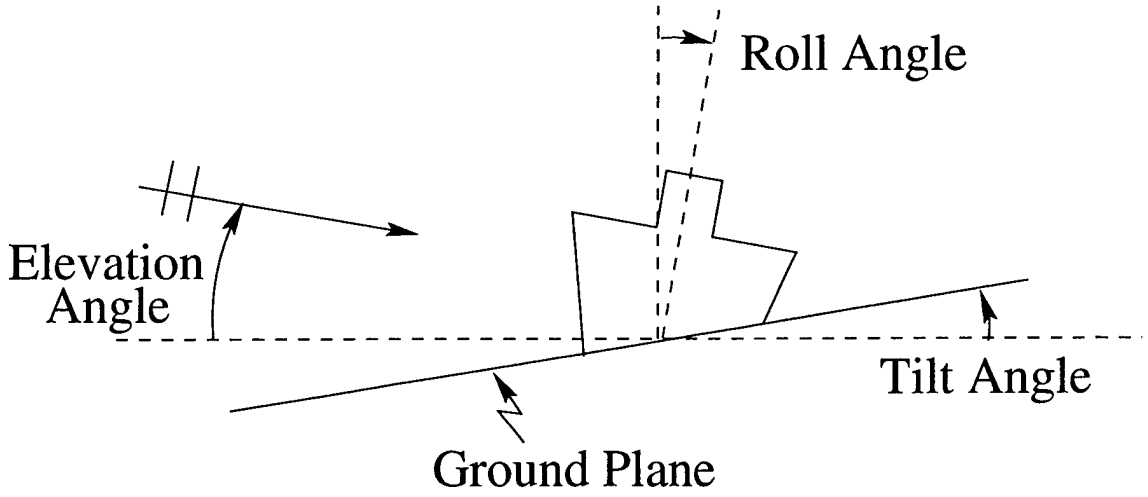

Figure 1.5: Tilted plane model for computing the RCS variations of a ship on a rough surface.

field combined with the local planar approximation for the sea surface effectively decouples the target scattering problem from the sea surface.

It was found in [1] that the discrete plane wave expansion could accurately reproduce the sea scattered field illuminating the ship, but the RCS computation could have significant errors. This is due to the fact that the incident field as found in Figure 1.3 satisfies a different surface boundary condition than in Figure 1.4. This introduces unwanted scattering effects which could, depending on the target geometry, cause the wrong conclusions to be reached about the RCS levels of a given target. This could be especially serious for low-observable targets.

Instead of trying to include the rough surface effect into the computation of the target RCS directly, it was found in [1] that the variations in the RCS caused by the rough surface could be predicted by studying the RCS of a target on a flat surface as a function of roll angle. This is because the sea surface locally in the vicinity of the target tends to look like a tilted flat plane, as shown in Figure 1.5. Since this problem can be easily solved using the flat surface Green's function, and in reality most surface targets will roll with the waves, the RCS vs. roll angle plot is a very useful tool for the ship designer. It is only necessary to know the maximum roll angle expected for a given target and sea state.

The second year study concluded the 2D analysis by considering the RCS of a target on a

time-evolving sea surface for very low grazing angles of incidence [2]. The low grazing case is of greatest practical interest because most detection problems involve a transmitter which is near the horizon (with the exception of look-down radars which may be satellite mounted). It had been shown that the variation in the RCS is small for low grazing angles because the incident field is highly coherent, but the RCS vs. time plots showed a significant variation in the RCS as the target moves up and down on the long ocean waves. The variations are apparently caused by shadowing of the incident field by the long ocean waves, and the changing slope of the long waves in the vicinity of the target. This added further confidence in the tilted plane model for predicting the variations in the RCS.

The 3D study was initiated in [2] with the analysis of the incident field in the presence of a spherical earth. It was found that the incident field illuminating a target that is before the horizon may be represented locally as an incident and reflected plane wave, but over the horizon the field becomes evanescent. To begin studying the scattering from 3D targets on a rough ocean surface, a rigorous and efficient method of moments reference solution was applied based on the multiple sweep method of moments (MSMM) [7, 8]. Some preliminary 3D scattering results were generated. One important distinction between 3D and 2D that became clear is that in 3D a significant cross-polarization component to the RCS can be introduced by the rough surface. Otherwise, it was observed that the conclusions reached in 2D generally applied to 3D as well. However, in the initial 3D investigation of the second year, only horizontal polarization was considered. The vertical polarization case is included in the third year. It is more challenging because the sea surface cannot be accurately modeled by a perfect electrical conductor (PEC) as done for horizontal polarization, so an impedance boundary condition must be implemented.

1.3 Third Year Study and Organization of Report

Some additional results from 2D are presented in Chapter 2. In the previous two reports [1, 2], only horizontal polarization was considered. Furthermore, a rigorous statistical analysis was not performed. Chapter 2 presents the results of a Monte Carlo simulation of the scattering

from a ship-like target on a rough sea surface as a function of elevation angle and wind speed. Both polarizations are considered, and the impedance boundary condition is used to model the sea surface for the vertical polarization case. With the statistical results, it is shown that the coherent scattering from the target cannot, in general, be predicted by illuminating the target with only the coherent component of the incident field.

Chapter 3 presents a large number of 3D scattering results for different target shapes, including both horizontal and vertical polarizations. The forward-backward iterative physical optics approach is used to generate the data. A small scale Monte Carlo simulation is included, followed by some plane wave/planar surface approaches for predicting the variations in the RCS due to the rough sea surface. The tilted plane model is one of these approaches, and is shown to be useful for predicting the co-polarized RCS variations, but not the cross-polarization. However, the rolling of the target is only computed in the plane of incidence; it is possible that other roll planes may give better results for cross-pol.

Chapter 4 continues to investigate the effect of a spherical earth on the incident field and the RCS of a 3D target. Interesting comparisons are presented for the scattering from the target on a flat and spherical earth. Some additional results computed using the parabolic wave equation are also presented. Vertical polarization is included, which had not been considered in [1] and [2].

General observations and conclusions are discussed in Chapter 5, along with a prescription for analyzing the RCS of marine targets using the ray-optical methods developed in this study. Suggestions for future work are also included.

Chapter 2

2D Monte Carlo Study

2.1 Introduction

In this chapter the results of a Monte Carlo study are presented for a two-dimensional (2D) ship-like target on a long ocean surface.[1] The generalized forward-backward (GFB) method that was used in [1] and [2] is again used to generate the numerical data [9, 10]. Here, the 2D RCS data (or, radar echo width) is generated for 21 random realizations of the rough sea surface for each wind speed. This allows the statistical properties of the RCS to be studied more thoroughly.

Figure 2.1 shows the dimensions of the 2D ship. The ship is placed close to the right end of a 400 m rough surface and the plane wave is incident from the left with elevation angle ϕ as shown in the figure. The ship may move up and down with the waves so that approximately the same hull surface area is exposed, but the ship does not roll on the waves. A low-observable 2D object is also analyzed in Section 2.3.

The ship is a perfect electrical conductor (PEC), and for horizontal polarization the sea surface is also modeled as a PEC. For vertical polarization the sea surface is modeled as an impenetrable impedance surface with surface impedance given by

$$Z_s = \sqrt{\frac{\mu_o}{\epsilon}} \quad ; \quad \epsilon = \epsilon_r \epsilon_o - j\frac{\sigma_c}{\omega} \tag{2.1}$$

where $\mu_o = 4\pi \times 10^{-7}$ h/m and $\epsilon_o = 8.854 \times 10^{-12}$ f/m are the permeability and permittivity

[1] The 2D numerical results were prepared by Dr. Marcos Rodriguez Pino and Prof. Fernando Obelleiro of the University of Vigo, Spain.

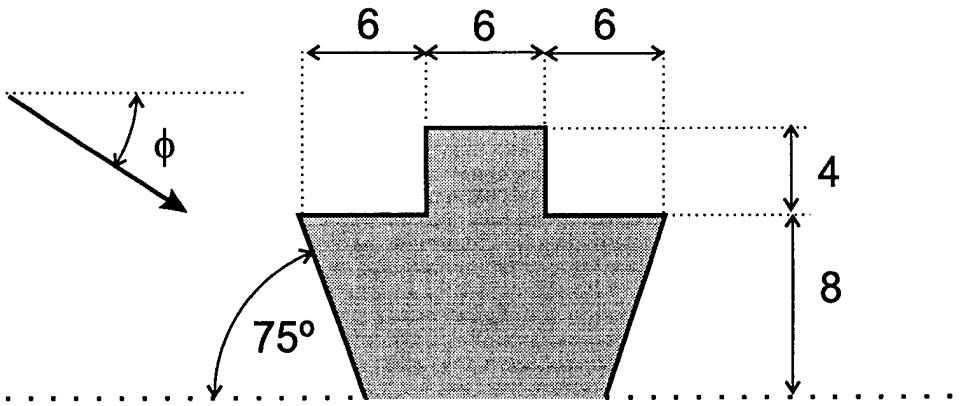

Figure 2.1: Dimensions of the 2D ship analyzed in the Monte Carlo study (in meters).

of free space, respectively, $\epsilon_r = 80$ is the relative permittivity (dielectric constant) of sea water, $\sigma_c = 4$ mho/m is the conductivity of sea water, and ω is the radian frequency of the time-harmonic electromagnetic field. In the numerical results which follow the frequency is 1 GHz at which the complex relative permittivity of sea water is $80 - j71.9$. For such a high dielectric constant and conductive lossiness, the impenetrable surface impedance model is very accurate for all angles of incidence at this frequency.

The rough surface is modeled as a zero-mean Gaussian random surface with a Pierson-Moscowitz infinite-depth ocean spectrum for a given wind speed [11]. The RMS roughness in meters is given in terms of the wind speed u in meters/second by the empirical relation

$$\hat{\sigma} = 0.0054u^2. \tag{2.2}$$

In the following, the average, coherent, and incoherent RCS curves are shown. These are defined in terms of the far zone scattered electric field $\bar{E}^s$ (with $1/\rho$ dependence suppressed) as

$$\begin{aligned} \text{Average RCS} &= 4\pi < |\bar{E}^s|^2 > \\ \text{Coherent RCS} &= 4\pi \mid < \bar{E}^s > \mid^2 \\ \text{Incoherent RCS} &= 4\pi \left(< |\bar{E}^s|^2 > - \mid < \bar{E}^s > \mid^2 \right) \end{aligned} \tag{2.3}$$

where $< \cdot >$ denotes the expected value computed over the entire sample for a given incidence angle and wind speed. The coherent RCS depends on the phase of the scattered field, so

it is always less than or equal to the average RCS which only depends on the magnitude. It is a measure of the time-averaged scattered field at the radar receiver for a target on a time-changing sea surface. The incoherent RCS is a measure of the amount of variation in the RCS. The average RCS is the sum of the coherent and incoherent RCS, and is the expected value of the RCS for a given elevation angle and wind speed.

2.2 Monte Carlo Results for 2D Ship

Figure 2.2 shows the average RCS results plotted over elevation angle and wind speed for the 2D ship. The figure shows that for low wind speeds or low elevation angles the average RCS is relatively independent of wind speed. This is made clearer in Figures 2.3 and 2.4 which show the coherent and incoherent RCS, respectively. For low wind speeds or low elevation angles the RCS is mostly coherent, whereas, for high wind speeds or elevation angles the RCS is incoherent.

These results are again explained by considering the coherence of the incident field as done in [1] and [2]. The incident field which illuminates the ship may be decomposed into the incident plane wave plus the scattering of the incident plane wave from the sea surface. The incident plane wave is coherent, but only a portion of the sea-scattered incident field is a coherent reflected plane wave. The analytic coefficient which determines the magnitude of the coherent reflected plane wave is given by [3]

$$\Gamma(\phi, k\hat{\sigma}) = e^{-2(k\hat{\sigma}\sin\phi)^2} \tag{2.4}$$

which is a function of the elevation angle ϕ, the wavenumber of the incident electromagnetic field k, and the RMS surface roughness $\hat{\sigma}$. (Note that this coefficient does not include the material reflection coefficient, which is also a factor in computing the coherent reflected plane wave.) For low elevation angles or small roughness, Γ is close to unity, which means the sea-scattered incident field is highly coherent. Figure 2.5 plots the curve $\Gamma = 0.25$ as a function of elevation angle and wind speed. When overlaid onto Figures 2.2-2.4, this curve tends to delineate the coherent and incoherent regions. It should be mentioned, however,

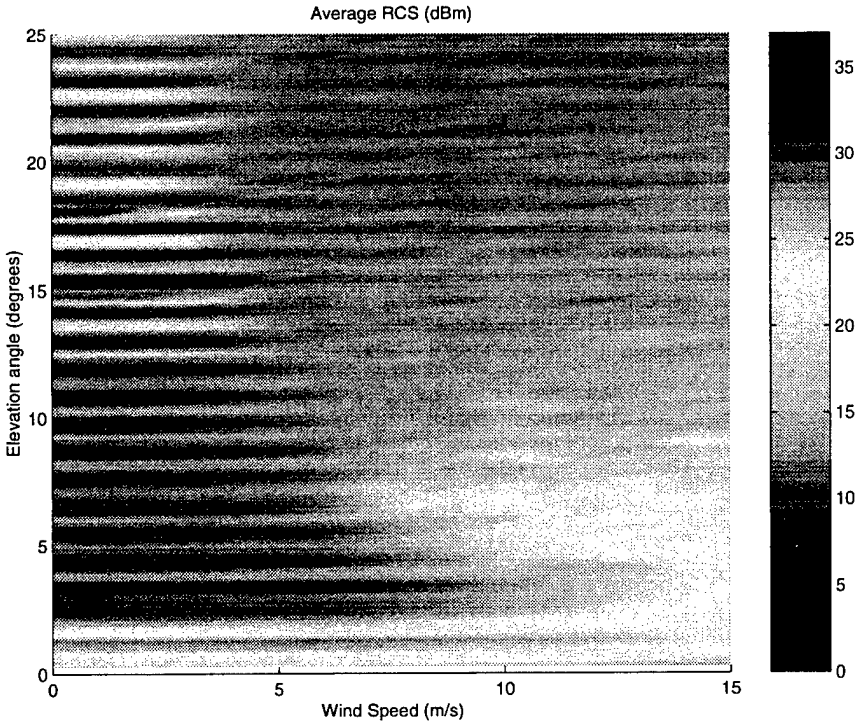

(a) Horizontal polarization.

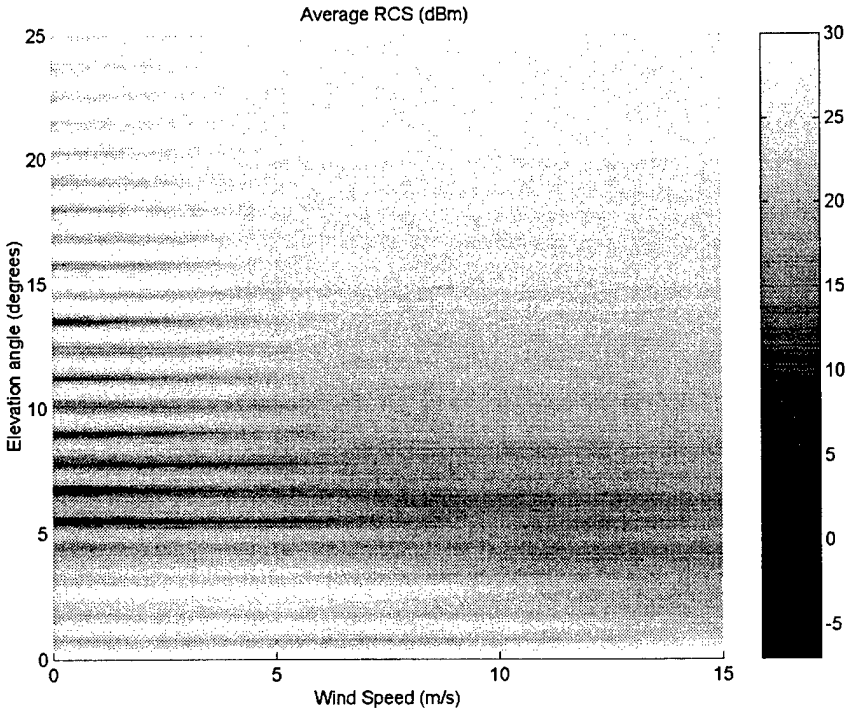

(b) Vertical polarization.

Figure 2.2: Average RCS of a 2D ship-like target as a function of wind speed and elevation angle. Frequency = 1 GHz.

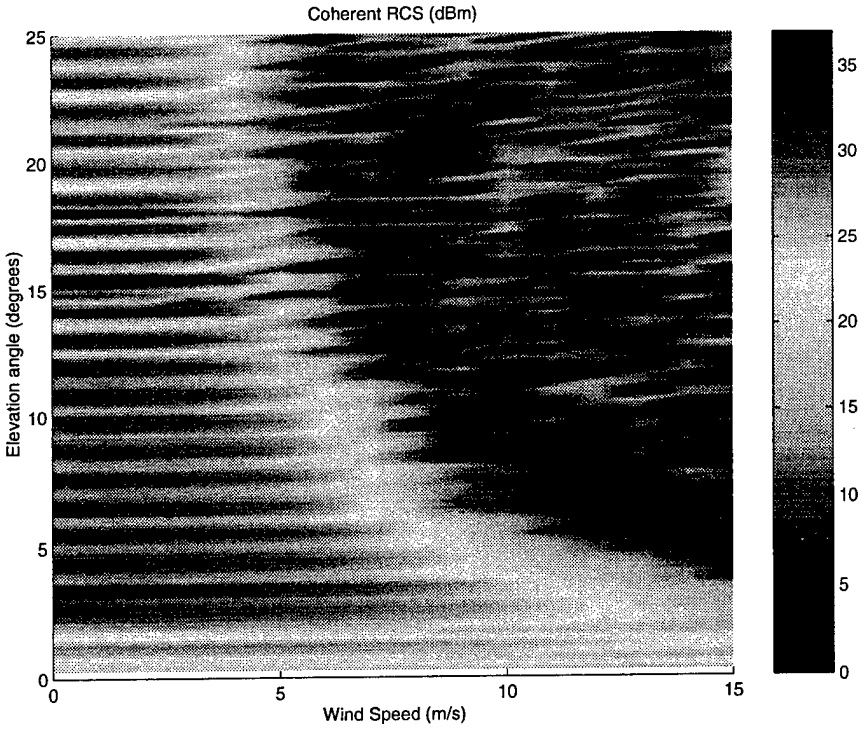

(a) Horizontal polarization.

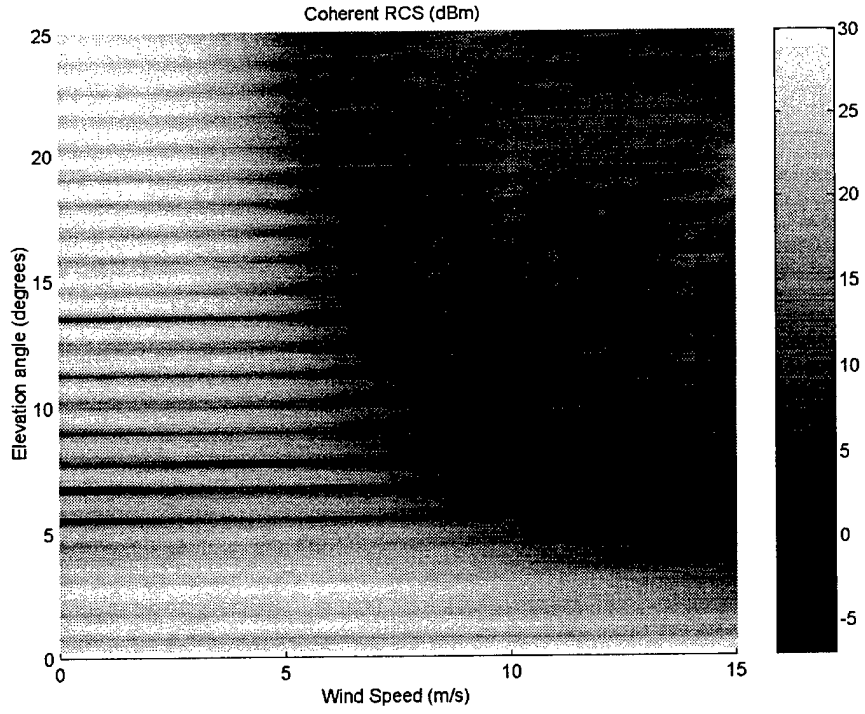

(b) Vertical polarization.

Figure 2.3: Coherent RCS of a 2D ship-like target as a function of wind speed and elevation angle. Frequency = 1 GHz.

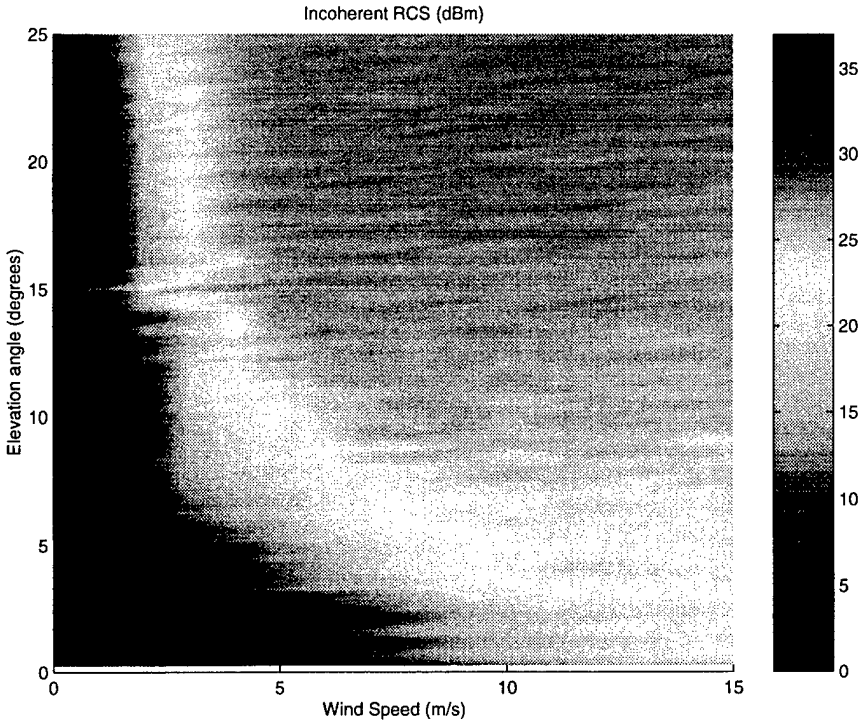

(a) Horizontal polarization.

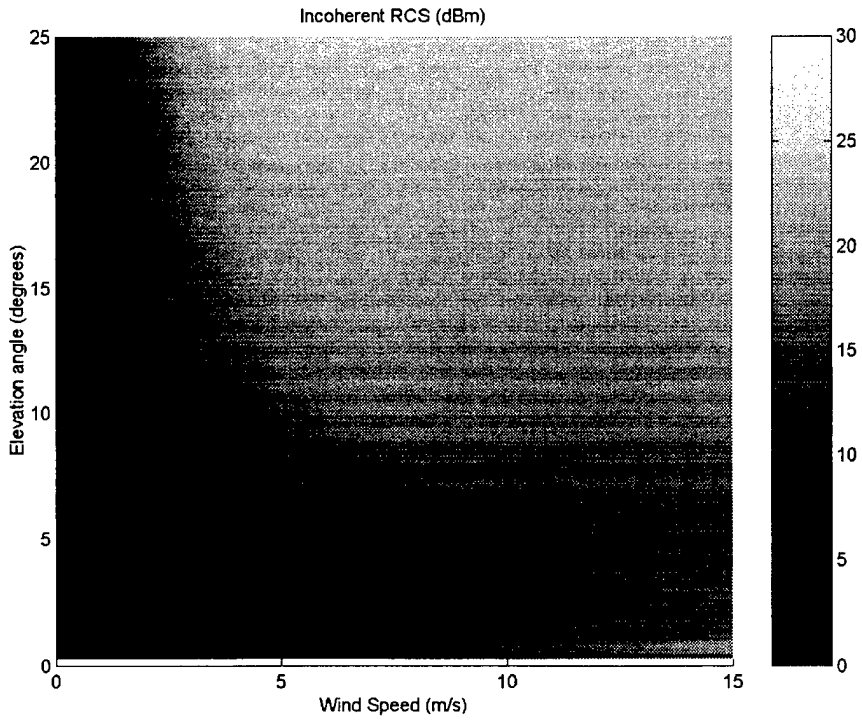

(b) Vertical polarization.

Figure 2.4: Incoherent RCS of a 2D ship-like target as a function of wind speed and elevation angle. Frequency = 1 GHz.

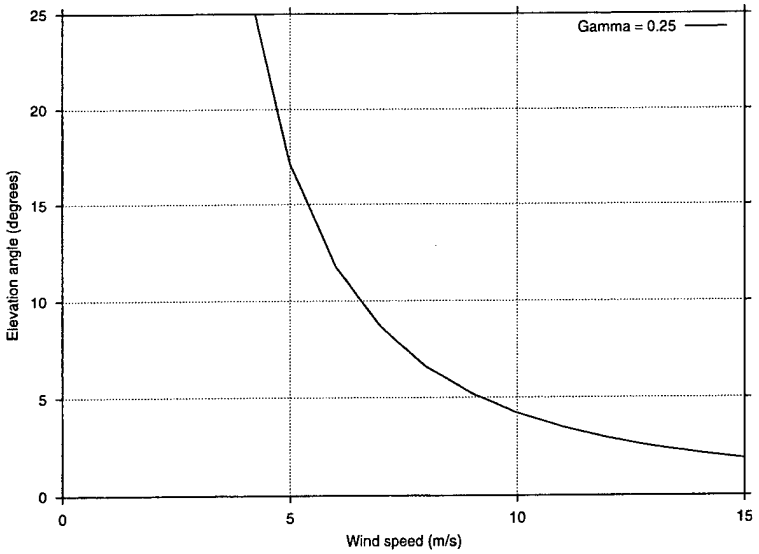

Figure 2.5: Plot of $\Gamma(\phi, k\hat{\sigma}) = 0.25$. Frequency = 1 GHz.

that the constant Γ of 0.25 was chosen to best fit the data, and the constant is expected to be dependent on the ship geometry [12]. It is also noted that some variations in the RCS are present even for low grazing angles when the incident field is highly coherent, as shown in the RCS vs. time plots of [2]. These variations appear to be due to the ship riding up and down on the long ocean waves.

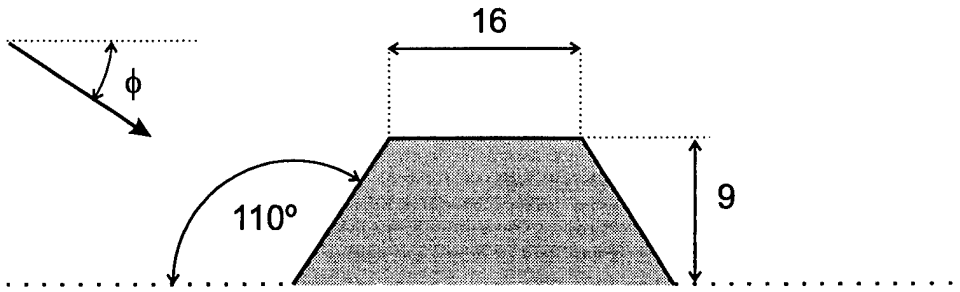

Figure 2.6: Dimensions of the 2D low-observable object analyzed in the Monte Carlo study (in meters).

2.3 Monte Carlo Results for Low-Observable Object

Figure 2.6 shows a low-observable 2D object which is placed on the same set of rough sea surfaces as the ship target of the last section. The object is PEC. Only horizontal polarization data is available for this target.

Figure 2.7 shows the average and incoherent RCS for the 2D low-observable object. Coherent RCS is not available at this time, but is the difference between the average and incoherent as given by Eq. (2.3). Please note that the axes are switched with respect to the results of the previous section. The results for this target show that the RCS is highly incoherent for high wind speeds and low elevation angles. The RCS is highly coherent for low wind speeds or for elevation angles near 20°. The strong peak around 20° is due to broadside illumination of the slanted side of the object. In this case the RCS is always high, and is not influenced much by the rough sea surface. For low elevation angles the RCS is about 40 dB lower than for broadside.

2.4 Coherent Incident Plane Wave Approach

Since it is very numerically intensive to compute the RCS of a target on rough surface by modeling a very large portion of the surface, one of the main directions of this research has been to investigate alternative methods. One approach first considered in [1] was to use the coherent portion of the incident field to illuminate the target. The target was placed on an infinite flat surface and illuminated with the rough surface coherent field. The approach did

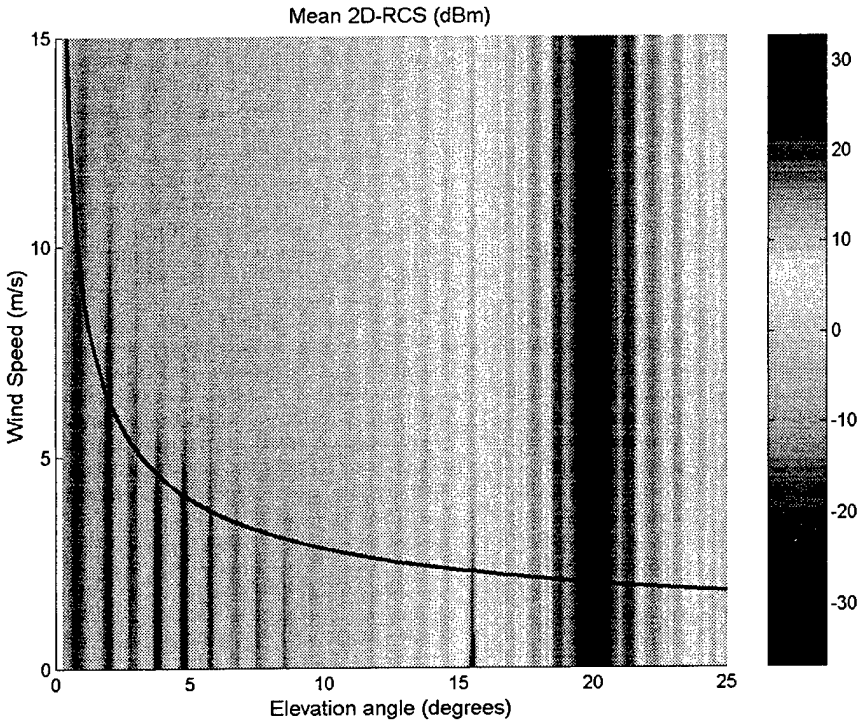

(a) Average RCS.

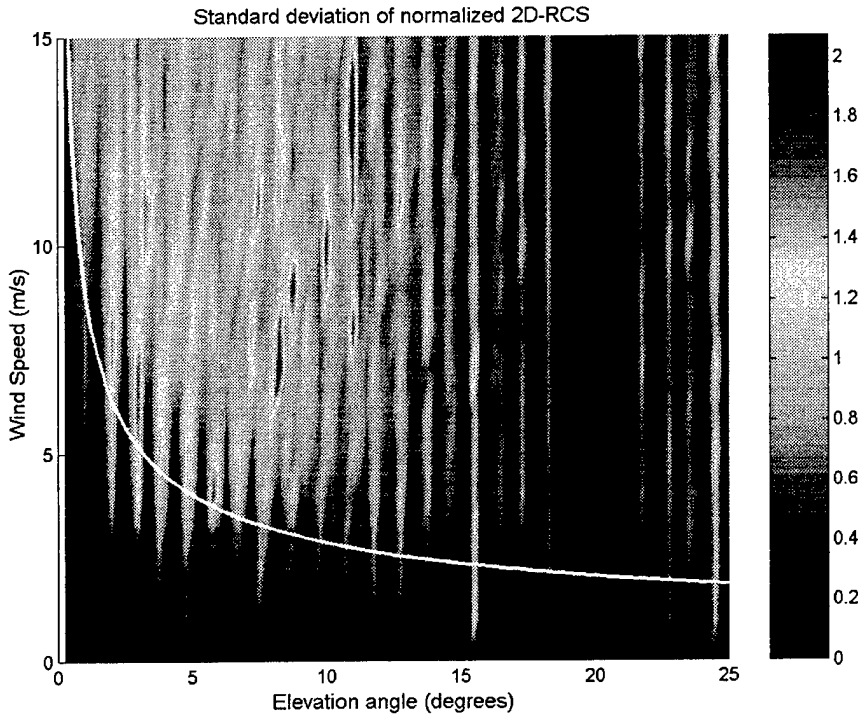

(b) Incoherent RCS.

Figure 2.7: Average and incoherent RCS of a 2D low-observable object as a function of wind speed and elevation angle. Horizontal polarization, Frequency = 1 GHz.

not predict well the scattering from the target on a single realization of a random rough surface because the incoherent portion of the incident field was missing, and the boundary condition at the sea surface was violated.

With the Monte Carlo results of this section it is possible to now check to see if the above approach can predict the coherent RCS. In other words, can the coherent RCS be predicted by illuminating the target with the coherent incident field? Figure 2.8 shows the results by comparing the coherent RCS patterns with the RCS computed from the coherent incident field for different wind speeds. For the coherent incident field results, the ship is placed on an infinite flat surface and illuminated by the incident and reflected plane waves, but the reflected plane wave is weighted by the coherent scattering coefficient Γ of (2.4). It is clear that the results are in good agreement only when the incident field is highly coherent, i.e., for low wind speeds or low elevation angles as expected. (The disagreement for low elevation angles is due to the finite surface model which limits the lowest elevation angle to about 2°.) Otherwise, the coherent incident field approach tends to over-predict the coherent RCS for this target geometry. Therefore, the coherent incident field approach it is not recommended. And as mentioned above, when the incident field does not include the incoherent sea-scattered field, the boundary condition at the sea surface interface is not satisfied. Furthermore, even if the boundary condition were satisfied on the rough surface, it would not be satisfied when the target is placed on a flat surface and illuminated with the same field.

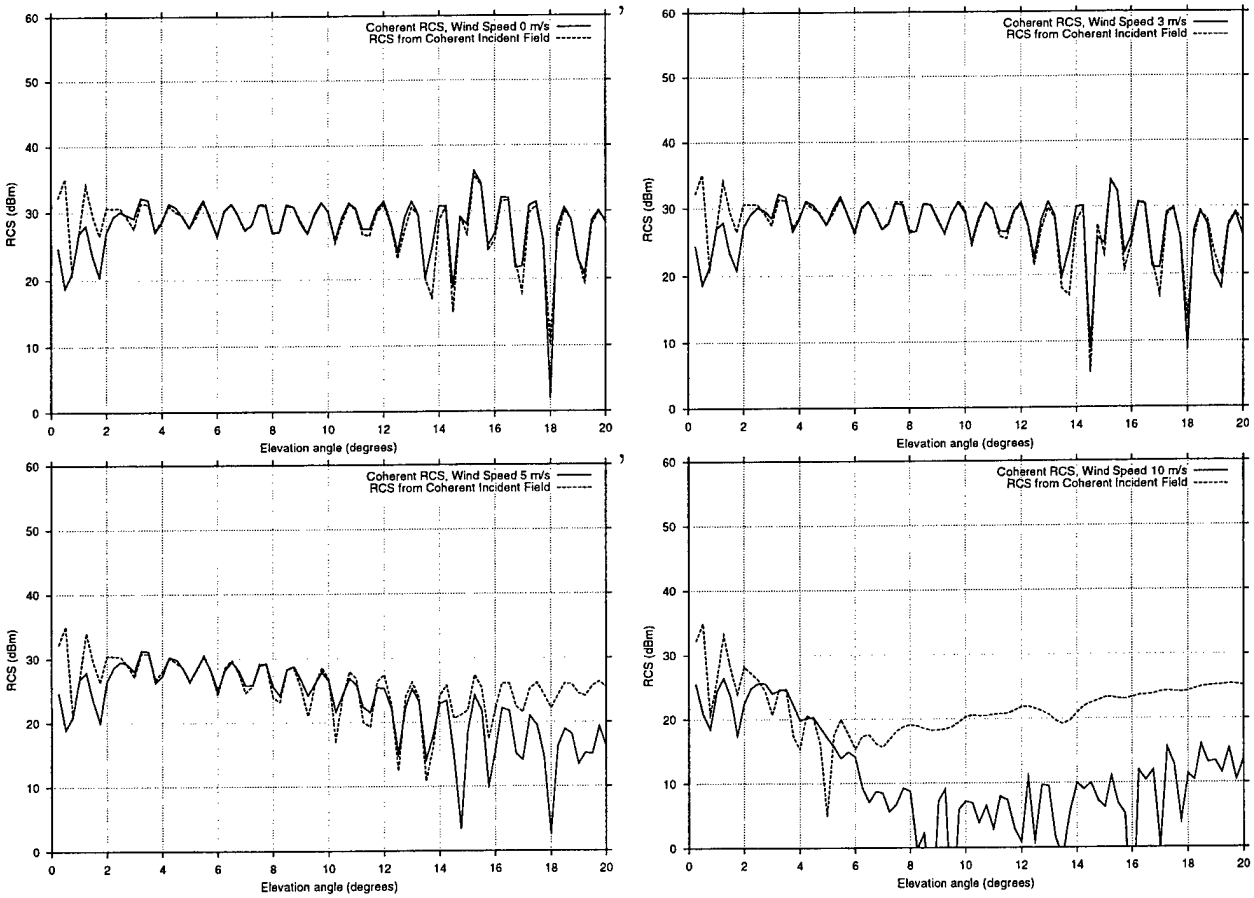

Figure 2.8: Coherent RCS patterns of a 2D ship-like target on a rough surface with different wind speeds compared with the RCS computed from the coherent incident field. Horizontal polarization. Frequency = 1 GHz.

Chapter 3

Numerical Study of Scattering from 3D Targets on a Rough Ocean Surface

3.1 Introduction

Numerical results are presented in this chapter to demonstrate the scattering characteristics of simple 3D targets on ocean-like rough surfaces. The results give considerable insight into the effect of the rough surface on the target RCS. The forward-backward Iterative Physical Optics (IPO) method [13, 14] is used for most of the computations so that relatively large geometries in terms of wavelength may be considered. The IPO method gives good accuracy consistent with the physical optics approximation [5, 6], and includes multiple interactions by iterating the magnetic field integral equation until a convergent solution is obtained.

As described in the previous chapter, the sea surface is modeled as an impenetrable impedance surface with surface impedance given by

$$Z_s = \sqrt{\frac{\mu_o}{\epsilon}} \quad ; \quad \epsilon = \epsilon_r \epsilon_o - j\frac{\sigma_c}{\omega} \tag{3.1}$$

where $\mu_o = 4\pi \times 10^{-7}$ h/m and $\epsilon_o = 8.854 \times 10^{-12}$ f/m are the permeability and permittivity of free space, respectively, $\epsilon_r = 80$ is the relative permittivity (dielectric constant) of sea water, $\sigma_c = 4$ mho/m is the conductivity of sea water, and ω is the radian frequency of the time-harmonic electromagnetic field. In the numerical results which follow the frequency is 1 GHz at which the complex relative permittivity of sea water is $80 - j71.9$. For such a high dielectric constant and conductive lossiness, the impenetrable surface impedance model is

very accurate for all angles of incidence at this frequency.

The rough surface is modeled as a zero-mean Gaussian random surface with a power law spectrum. The spatial high-frequency cut-off is held constant and the low-frequency cut-off is varied to obtain the desired RMS roughness of the surface. This is very similar to the Pierson-Moscowitz spectrum for modeling the ocean surface, where increasing wind speed gives rise to longer wavelength ocean waves and larger RMS roughness. The RMS roughness is given by the empirical relation

$$\hat{\sigma} = 0.0054u^2 \tag{3.2}$$

where $\hat{\sigma}$ is in meters and u is the wind speed in meters/second. It is noted that the ocean spectrum is omni-directional, independent of the wind direction.

Section 3.2 shows numerical results which demonstrate the effects of different wind speeds and azimuth angles on the RCS of simple block targets on deterministic ocean-like rough surfaces. Section 3.3 presents the results of a small-scale Monte Carlo simulation for two simple 3D targets on a random set of rough surfaces, and Section 3.4 demonstrates the capabilities and shortcomings of some ray-optical approaches. In the following, horizontal polarization refers to the electric field in the $\hat{\phi}$ direction, and vertical polarization refers to the $\hat{\theta}$ direction.

3.2 Effects of Wind Speed and Azimuth Angle

This section presents RCS results for simple block targets on an ocean-like rough surface. The wind speed, azimuth angle and target geometry are varied. Figure 3.1 shows a 2-block target on a finite model of the ocean surface for wind speeds of 3 m/s and 5 m/s (RMS wave height $\hat{\sigma} = 0.0486$ m and $\hat{\sigma} = 0.135$ m, respectively). The large bottom block is a 0.9 m cube, and the smaller top block is a 0.45 m cube. At 1 GHz the target is 4.5 wavelengths tall and 3 wavelength wide, and the surface is 33x33 wavelengths. A realistic ship would have dimensions of hundreds or thousands of wavelengths at this frequency. Therefore, the scattering would be dominated by high-frequency mechanisms. Even though our simple block target is nowhere near that large, it is electrically large enough so that the scattering will dominated by high-frequency mechanisms similar to a more realistic geometry. It is noted that the results of this section are for single realizations of a Gaussian random surface for each wind speed and are intended only to demonstrate the accuracy of the finite surface model and trends in the RCS patterns; the Monte Carlo simulation of the next section considers multiple random samples of a rough surface for a given wind speed.

3.2.1 Validation of Finite Surface Model and IPO Approach

In the numerical results which follow, the illuminating plane wave is incident from the left so that the incident field sees a large area of the sea surface in front of the target. The reflected field from the sea surface which illuminates the target then approximates the scattering from an infinite sea surface as long as the elevation angle is not close to grazing. To reduce the effect of the finite sea surface, the direct scattering from the edges of the surface is removed by a subtraction procedure. The field scattered from the surface with the target absent is subtracted from the field scattered with the target present. This, by definition, extracts the scattering due to the presence of the target, and approximates the scattering from the target on an infinite surface.

The upper limit on the elevation angle is approximately the arctangent of target height divided by the length of the surface towards the source of the incident field, which in this case

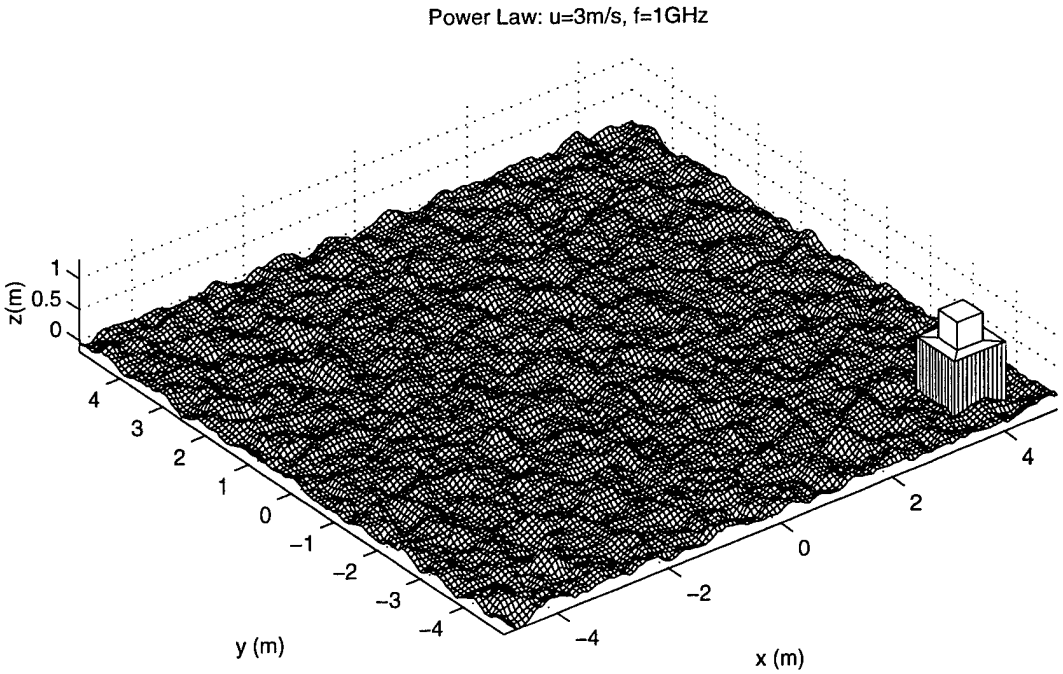

(a) Wind speed = 3 m/s.

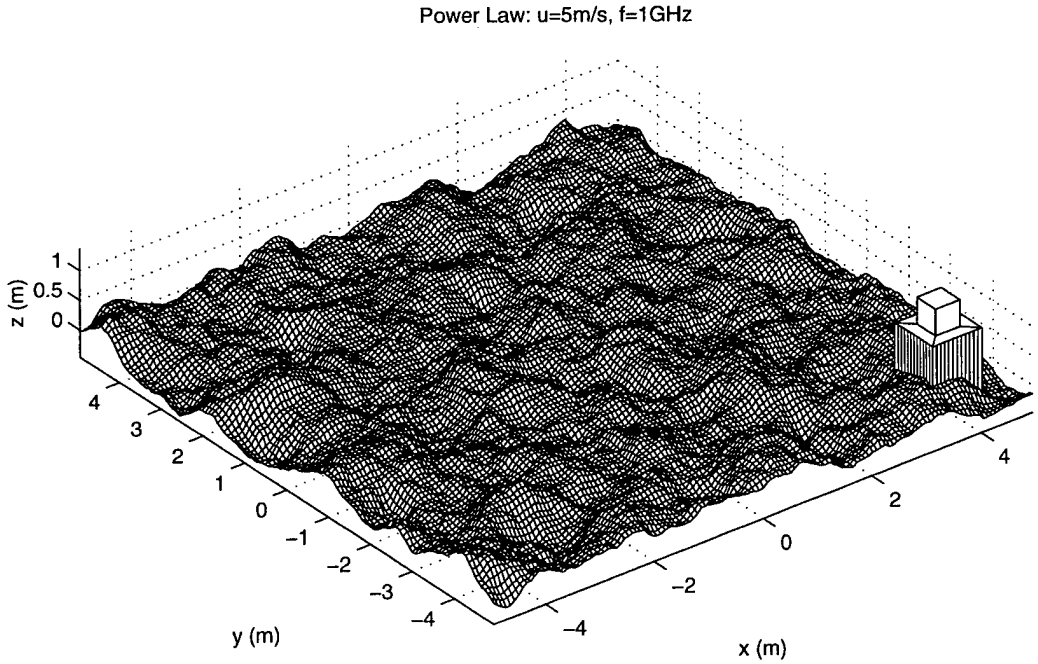

(a) Wind speed = 5 m/s.

Figure 3.1: 2-block target on a finite rough ocean surface for two different wind speeds.

is about 9°. Therefore, the RCS results for the finite surface of Figure 3.1 should simulate the infinite surface for incidence angles in the range $-81° < \theta < 0°, 0° \leq \phi \leq 90°$ in spherical coordinates.

To test the accuracy of the finite surface model and the subtraction approach, Figures 3.2 and 3.3 plot the RCS patterns in the $\phi = 0°$ and $\phi = 45°$ planes, respectively, of a 0.9 m 1-block target on a flat sea surface. The finite surface RCS is compared with the RCS of the block on an infinite surface. The infinite surface results are computed by illuminating the target with an incident and sea-reflected plane wave and using physical optics to find the equivalent scattered currents on the target. The backscattered field is then found using the reciprocity approach described in [1]. Since both results are based on physical optics, the accuracy is expected to be the same except for the effect of the finite surface in the IPO results. As the figures show, the patterns are in good agreement for $\theta > -81°$, as predicted.

Comparing Figures 3.2 and 3.3 it is clear that the broad side azimuth RCS levels are much higher than the 45° azimuth case. This is because in the broadside case the incident field sees a strong 90° corner reflector scattering mechanism formed by the side of the target and the sea surface. It is interesting to note in the results of Figure 3.2(b) that a notch occurs in the patterns close to $\theta = -84°$ for vertical polarization. This is close to the Brewster angle for sea water. Near this angle of incidence the reflection from the sea surface is very small, so the corner reflector formed by the side of the target and the sea surface is no longer a strong scattering mechanism.

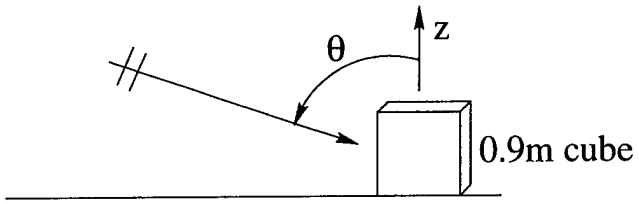

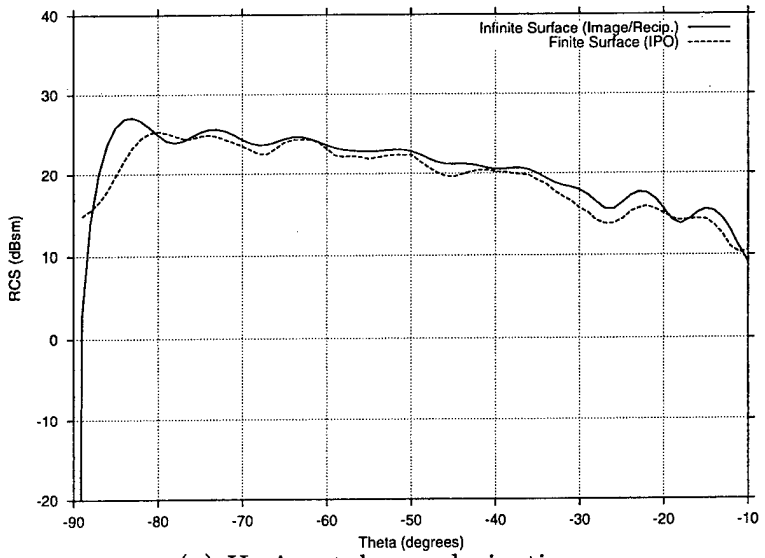

(a) Horizontal co-polarization.

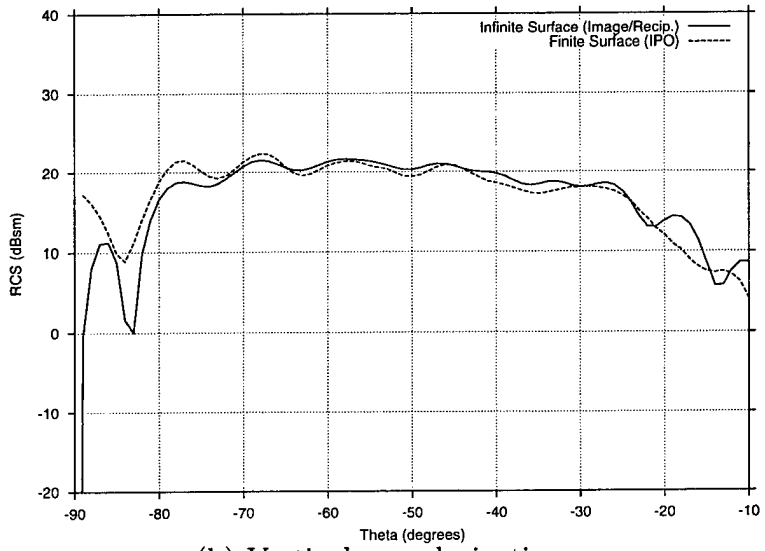

(b) Vertical co-polarization.

Figure 3.2: RCS vs. θ patterns for a 1-block target on a flat sea surface. Frequency = 1 GHz, $\phi = 0°$.

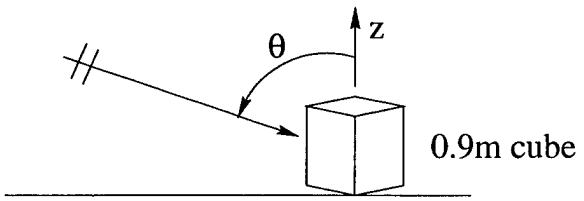

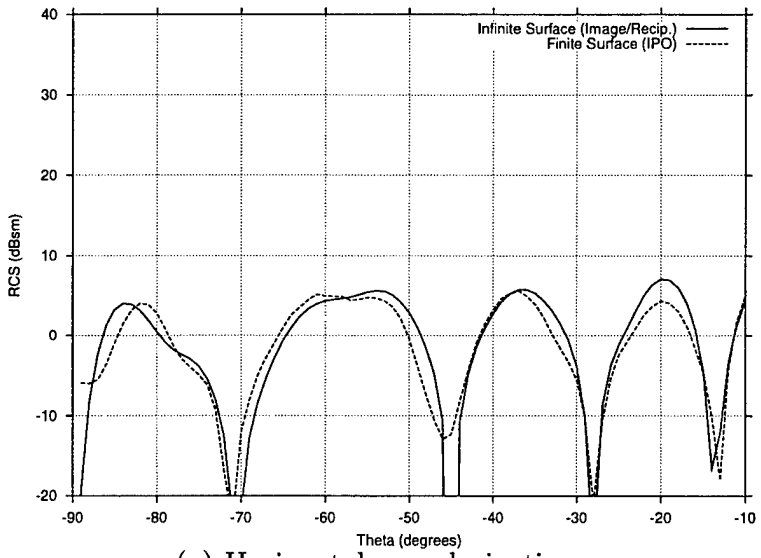

(a) Horizontal co-polarization.

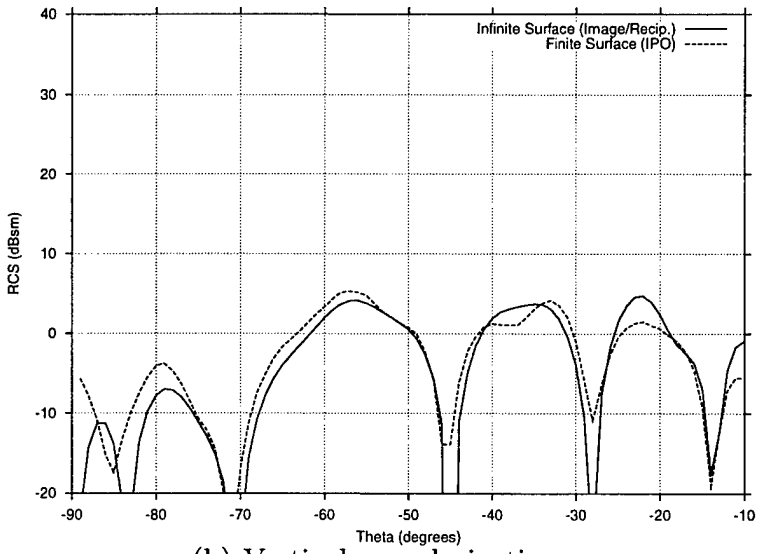

(b) Vertical co-polarization.

Figure 3.3: RCS vs. θ patterns for a 1-block target on a flat sea surface. Frequency = 1 GHz, $\phi = 45°$.

To further test the IPO approach, the IPO results for a smaller target and surface geometry were generated and compared with a rigorous method of moments (MoM) solution as described in Chapter 4 of [2]. The geometry tested is shown in Figure 4.1 of that report for a wind speed of 3.4 m/s and a frequency of 300 MHz. For this result the sea surface is PEC because a MoM reference solution is currently not available for an impedance sea surface with a PEC target. The extracted target RCS comparison is shown in Figure 3.4. The agreement is very good considering that the geometry is not nearly as large in terms of wavelengths as the geometries considered here.

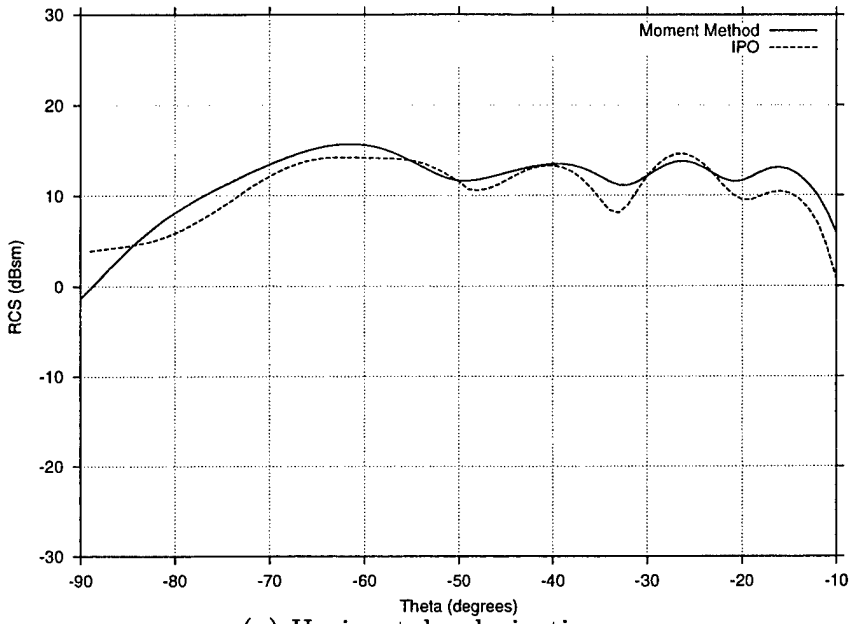

(a) Horizontal polarization.

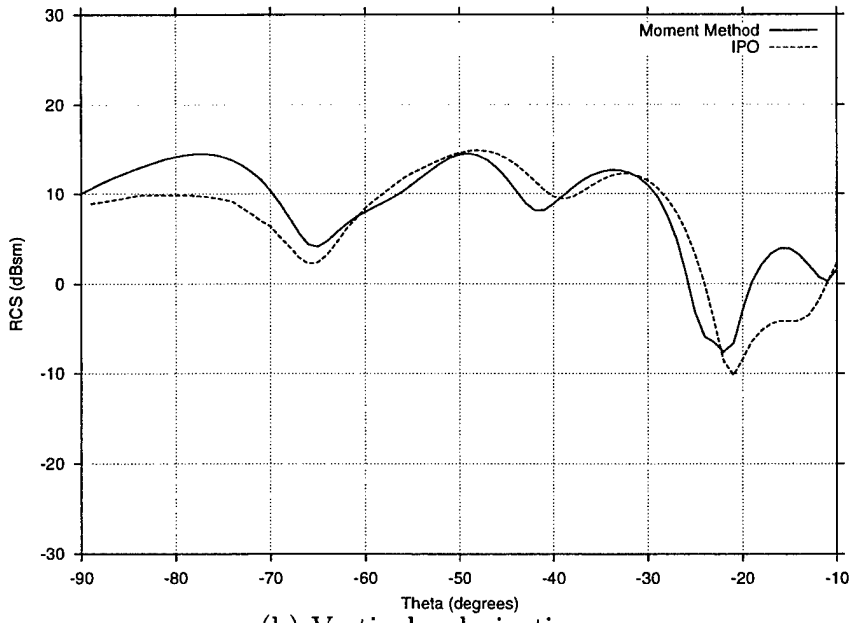

(b) Vertical polarization.

Figure 3.4: RCS vs. θ patterns for the block target of Figure 4.1 in [2]. Frequency = 300 MHz, $\phi = 0°$, wind speed = 3.4 m/s.

3.2.2 2-Block Target Results for Multiple Wind Speeds

Figure 3.5 shows the RCS patterns of the 2-block target of Figure 3.1 for different wind speeds and a horizontally polarized incident field in the $\phi = 0°$ plane. Cross-polarization results are also shown because the rough surface introduces a cross-polarization component to the target scattered field which is negligable for a flat surface. It is seen in the co-polarization results of Figure 3.5(a) that higher wind speeds tend to lower the RCS levels. This is because as the surface gets rougher the 90° corner reflector effect is broken up. It is also noticed that rough surface curves tend to converge to the flat surface curve as the incidence angle approaches $-90°$, as in the ealier 2D study. This is consistent with rough surface scattering theory because the coherent plane wave reflection coefficient from a rough surface approaches unity for low grazing angles.

The cross-polarization results of Figure 3.5(b) also indicate that, in general, higher wind speeds introduce a larger cross-pol component as would be expected. For this target and azimuth angle the cross-pol levels are generally much lower than co-pol, although at the highest wind speed considered they are comparable for some elevation angles.

Figure 3.6 shows the corresponding co- and cross-pol patterns for a vertically polarized incident field in the $\phi = 0°$ plane. Again it is seen that, in general, higher wind speeds cause a lower co-pol return and a higher cross-pol return. However, unlike the H-pol case, the V-pol co-polarization curves do not all tend to converge to the flat surface curve for low elevation angles. In fact, the two highest wind speeds converge together, but not to the flat surface result. This effect is not currently understood because it did not appear in the 2D results. It is possible that it is a non-physical artifact associated with the finite surface model or the IPO approximation. To eliminate the finite surface possibility, the same geometry was tested with a tapered beam incident field which did not illuminate the edges of the surface. The effect was still observed. Given that the IPO has been validated for a rough PEC surface with target in Figure 3.4, and for a flat impedance surface with target in Figures 3.2 and 3.3, it is unlikely that IPO is responsible for the effect. It is therefore most likely that the effect is physical, and will hopefully be independently validated in the future by measurements or

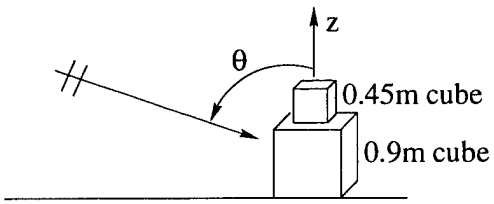

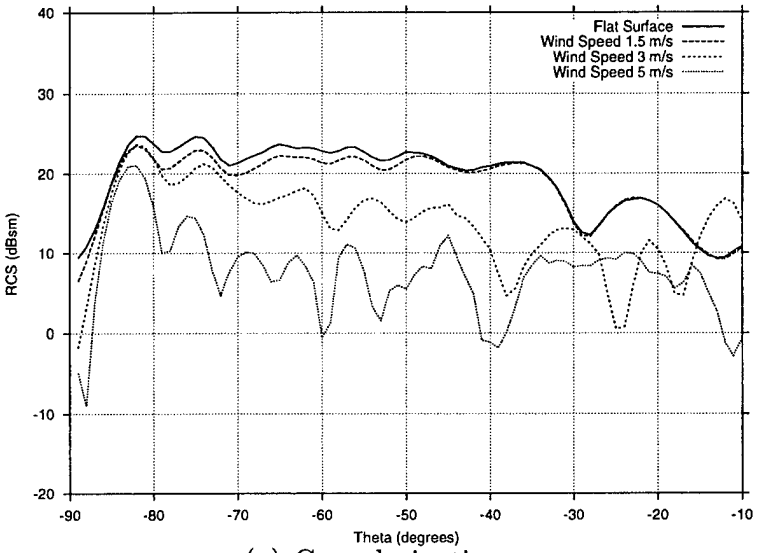

(a) Co-polarization.

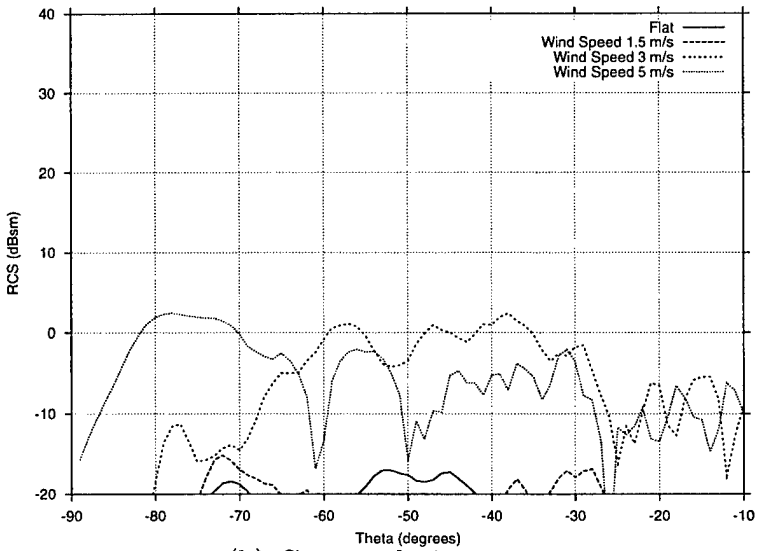

(b) Cross-polarization.

Figure 3.5: RCS vs. θ patterns for a 2-block target on a sea surface for different wind speeds. Incident field is horizontally polarized. Frequency = 1 GHz, $\phi = 0°$.

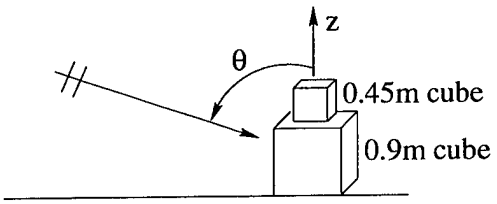

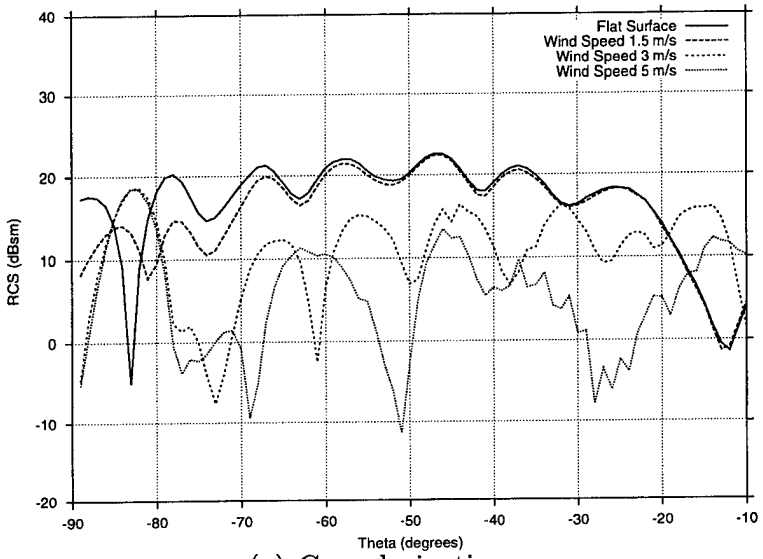

(a) Co-polarization.

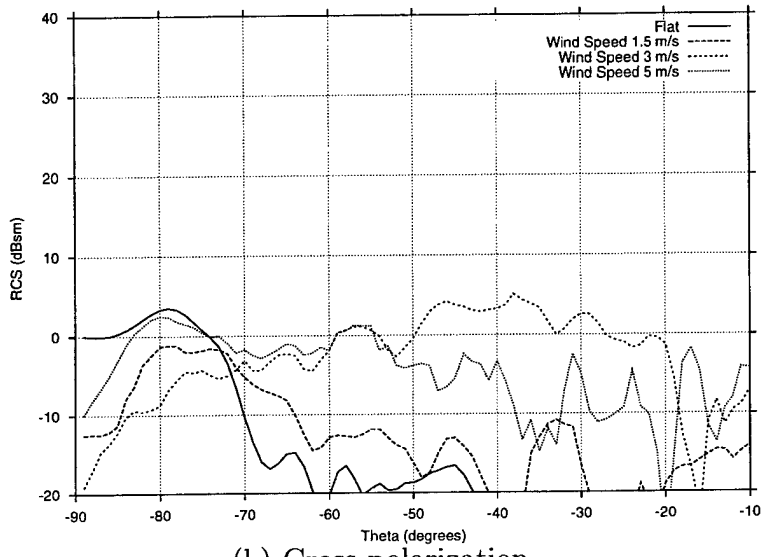

(b) Cross-polarization.

Figure 3.6: RCS vs. θ patterns for a 2-block target on a sea surface for different wind speeds. Incident field is vertically polarized. Frequency = 1 GHz, $\phi = 0°$.

a rigorous numerical solution that includes a rough impedance sea surface.

If the effect is real, since the unexplained effect occurs near the Brewster angle and only for vertical polarization, it is probable that the effect is related to the reflection coefficient of sea water. The reflection from a flat sea surface near the Brewster angle is very small, hence a notch was seen in the RCS patterns at this angle for the infinite flat surface of Figure 3.2(b). It is possible that the rough surface somehow breaks up the Brewster angle effect because the V-pol reflection coefficient is rapidly varying near this angle.

Figures 3.7 and 3.8 show the corresponding RCS patterns in the $\phi = 45°$ plane. Compared with the broadside incidence case, the co-pol patterns show that the rough surface does not in general lower the RCS levels, and actually increases the RCS for some angles. Also, the cross-pol component introduced by the rough surface is nearly as high as the co-pol levels. Again it is seen that the rough surface curves tend to converge to the flat surface curve for low elevation angles for horizontal polarization, but not for vertical polarization, so the same Brewster angle effect is present for this azimuth direction.

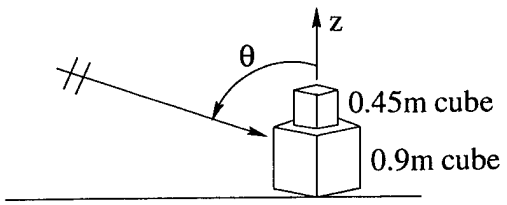

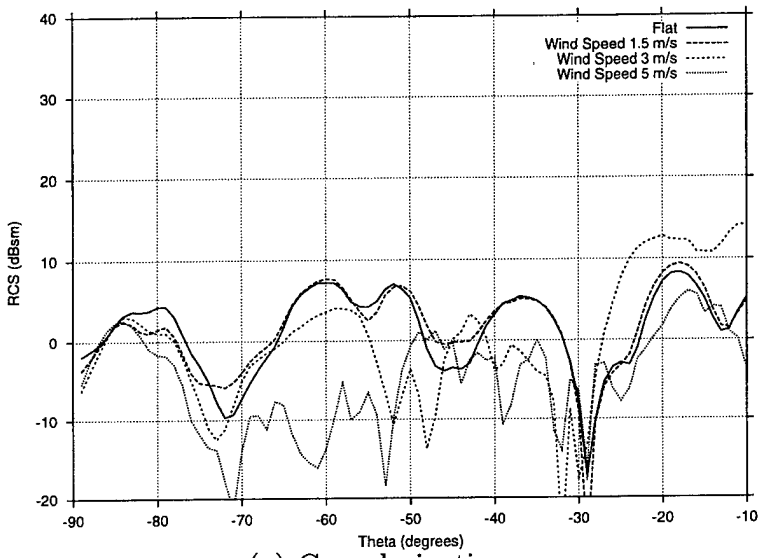

(a) Co-polarization.

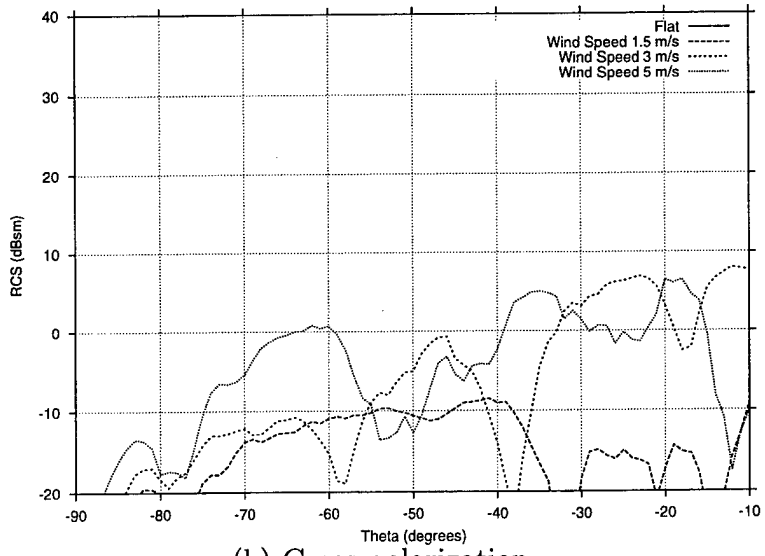

(b) Cross-polarization.

Figure 3.7: RCS vs. θ patterns for a 2-block target on a sea surface for different wind speeds. Incident field is horizontally polarized. Frequency = 1 GHz, $\phi = 45°$.

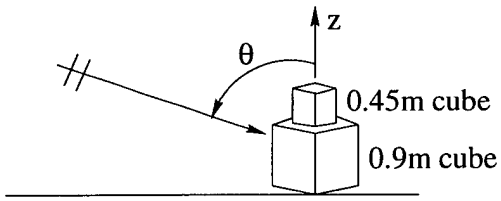

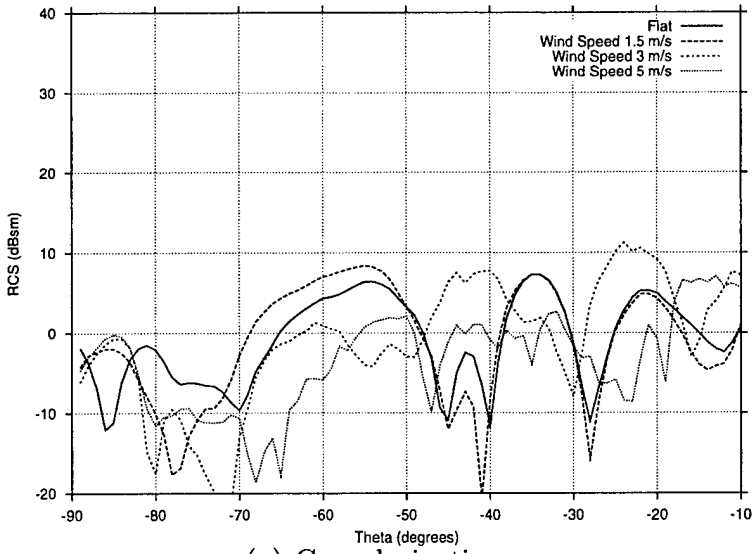

(a) Co-polarization.

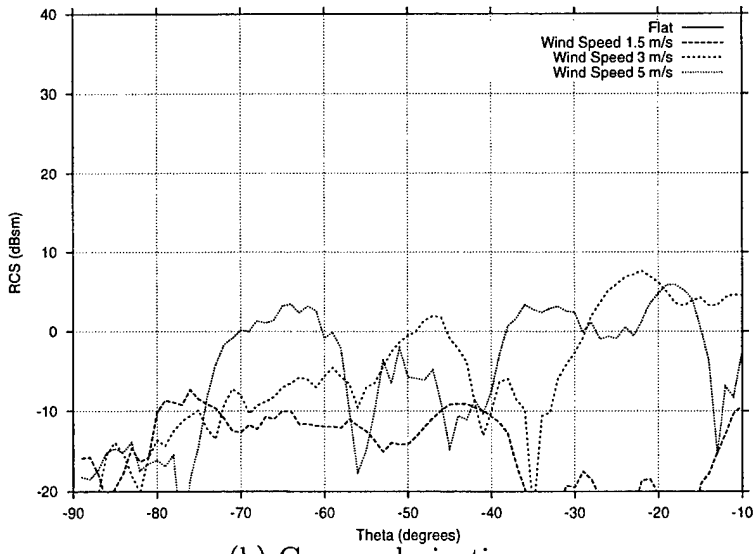

(b) Cross-polarization.

Figure 3.8: RCS vs. θ patterns for a 2-block target on a sea surface for different wind speeds. Incident field is vertically polarized. Frequency = 1 GHz, $\phi = 45°$.

3.2.3 RCS Patterns for an Inverted Trapezoidal Target

Figures 3.9 and 3.10 show the RCS vs. θ plots of an inverted trapezoidal target. The finite sea surface is 10x10 m as in Figure 3.1, and the target has the same dimensions as the 0.9 m cube target, but the sides which were parallel to the y-z plane are now slanted outward 14°. The sides parallel to the x-z plane are not slanted. This target is of interest because many ships may have outward slanted hulls instead of vertical or inward slanted hulls. It is seen that the RCS levels are considerably lower than the block target of Figure 3.2, except near $\theta = -75°$ for the horizontal co-pol case. This is close to the angle where the sea-reflected incident field illuminates the side of the trapezoid broadside. The horizontal co-pol case also shows convergence of the two wind speed curves as the elevation angle approaches grazing, as before. However, the vertical co-pol curves do not show the same behavior. The expected peak near $\theta = -75°$ is not present, and the co-pol curves do not converge for low elevation angles. This may again be due to the Brewster angle effect.

Figures 3.11 and 3.12 show the corresponding RCS vs. ϕ azimuth angle plots for the inverted trapezoid for an elevation angle of $\theta = -50°$. The results show that the rough sea surface can significantly increase the RCS levels, especially for azimuth angles away from broadside. It is also seen that the cross-pol levels may be comparable to co-pol.

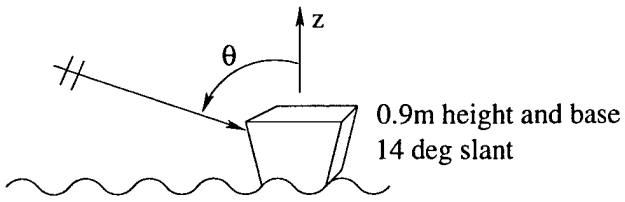

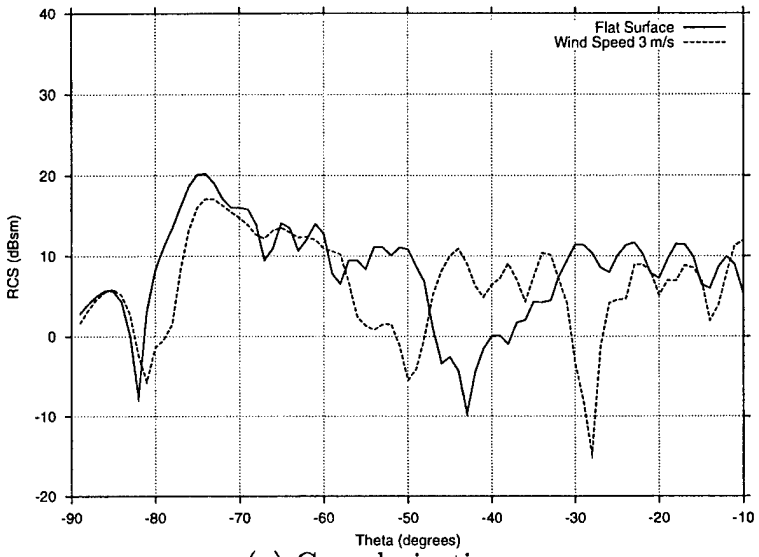

(a) Co-polarization.

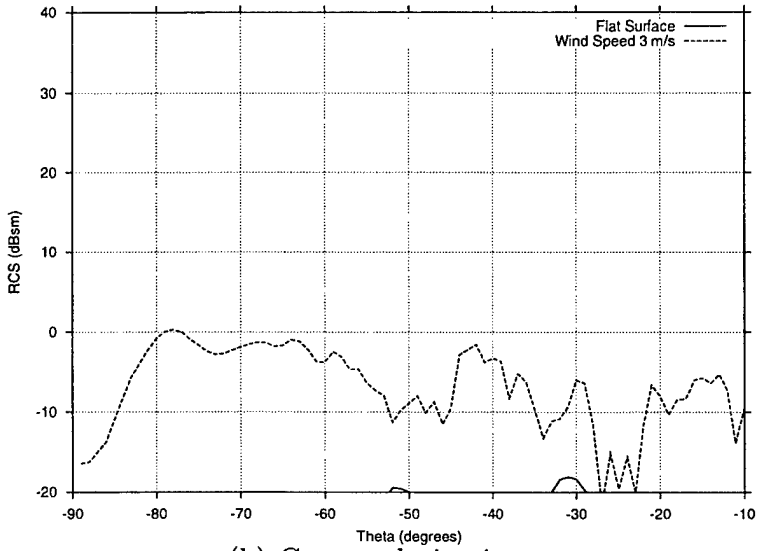

(b) Cross-polarization.

Figure 3.9: RCS vs. θ patterns for an inverted trapezoidal target on a sea surface for different wind speeds. Incident field is horizontally polarized. Frequency = 1 GHz, $\phi = 0°$.

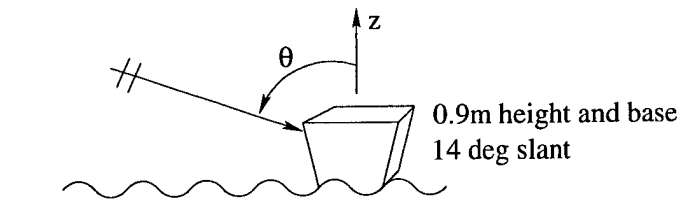

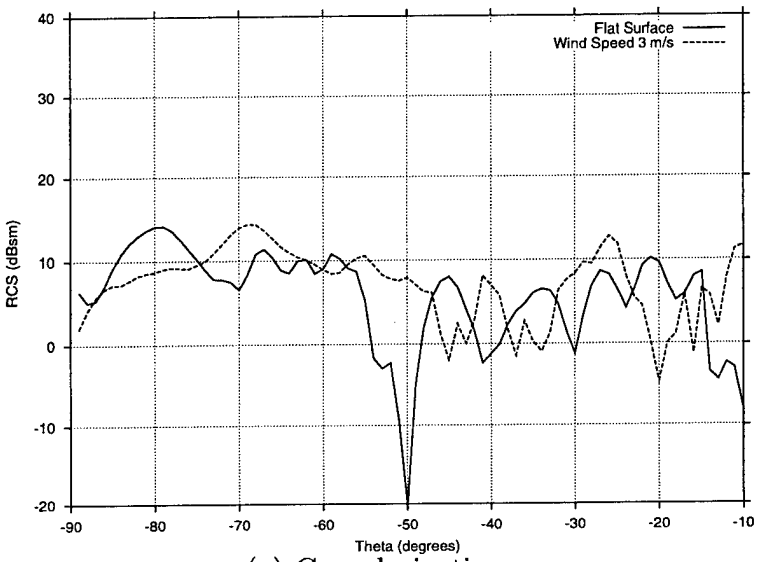

(a) Co-polarization.

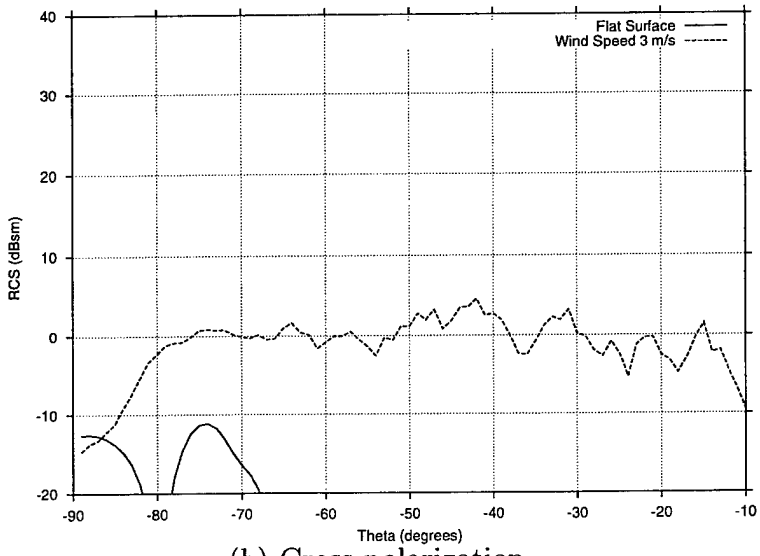

(b) Cross-polarization.

Figure 3.10: RCS vs. θ patterns for an inverted trapezoidal target on a sea surface for different wind speeds. Incident field is vertically polarized. Frequency = 1 GHz, $\phi = 0°$.

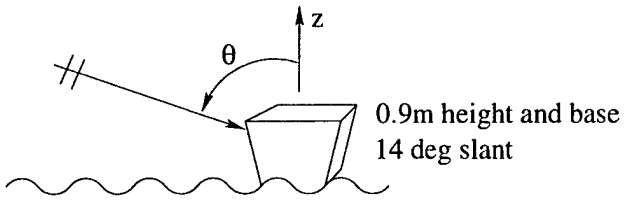

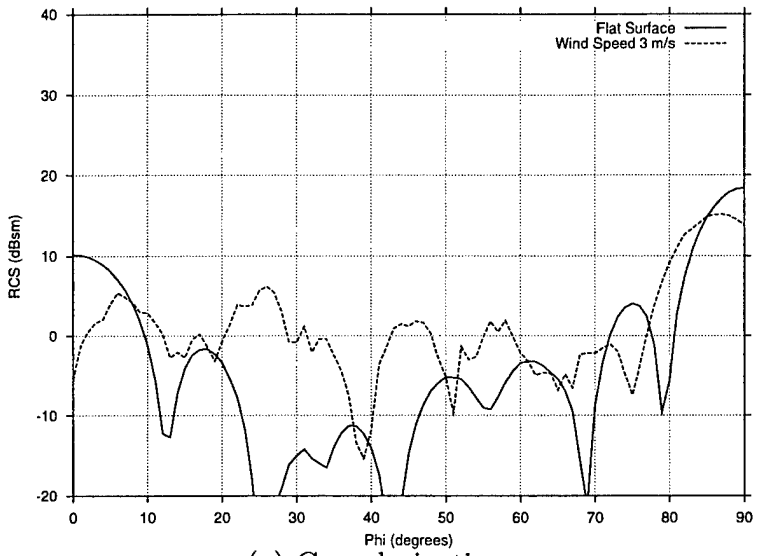

(a) Co-polarization.

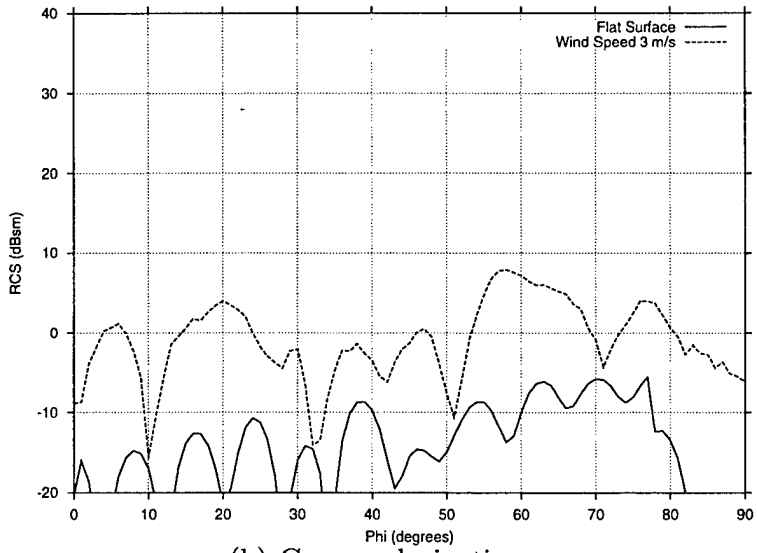

(b) Cross-polarization.

Figure 3.11: RCS vs. ϕ azimuth patterns for an inverted trapezoidal target on a sea surface for different wind speeds. Incident field is horizontally polarized. Frequency = 1 GHz, $\theta = -50°$.

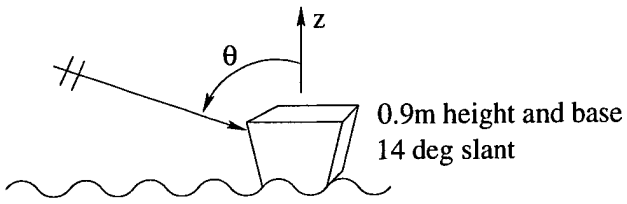

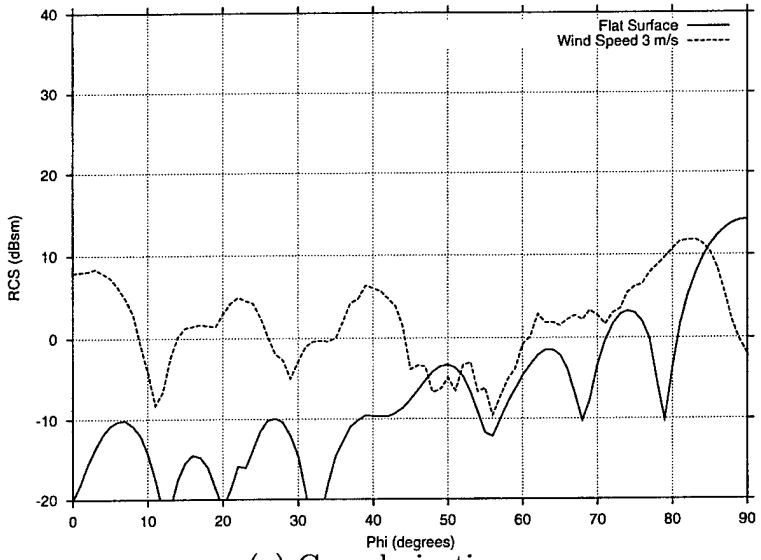

(a) Co-polarization.

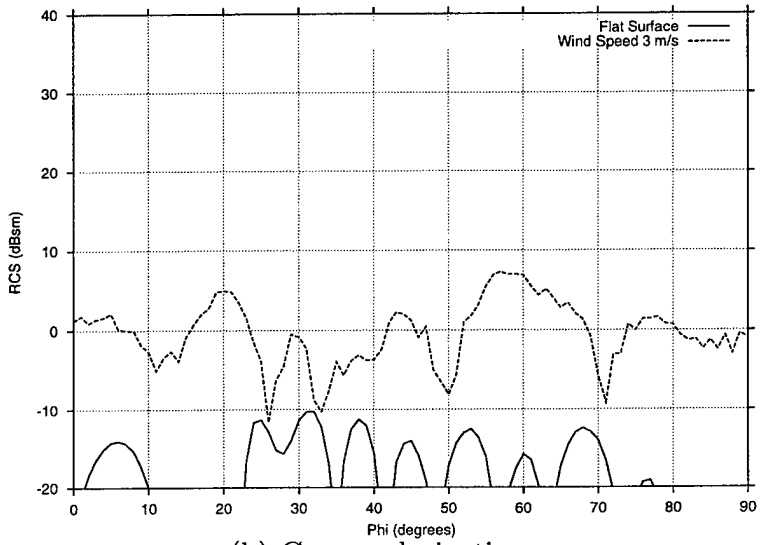

(b) Cross-polarization.

Figure 3.12: RCS vs. ϕ azimuth patterns for an inverted trapezoidal target on a sea surface for different wind speeds. Incident field is vertically polarized. Frequency = 1 GHz, $\theta = -50°$.

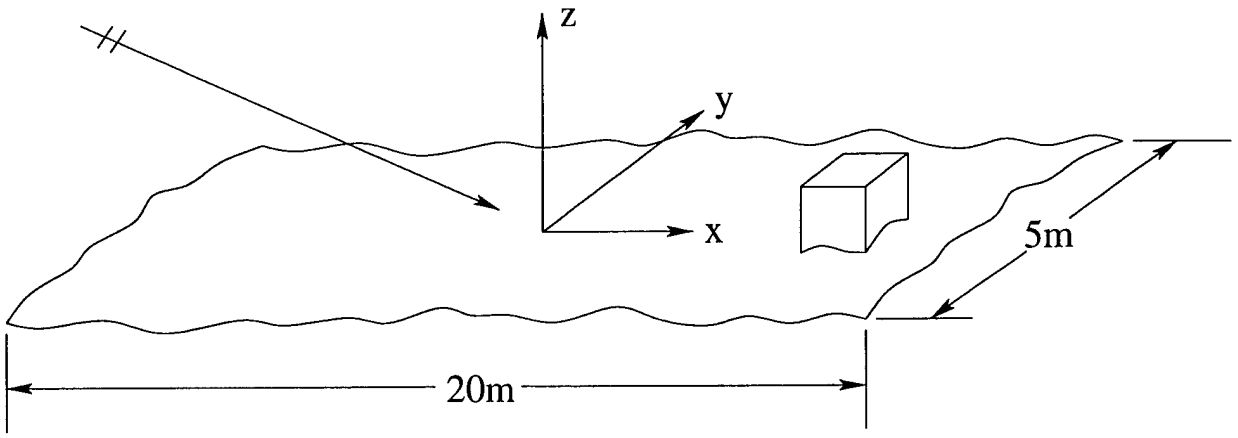

Figure 3.13: 0.9 m cube target and surface geometry for the Monte Carlo simulation. Wind speed is 3 m/s.

3.3 Monte Carlo Study

The RCS results of the previous section were for single realizations of a Gaussian random surface with differing RMS roughness (wind speed). In this section a more thorough Monte Carlo statistical analysis is performed for a sampling of randomly generated rough sea surfaces with the same wind speed. This allows coherent and incoherent components of the RCS to be identified.

3.3.1 0.9 m Cube Target

Figure 3.13 shows the first geometry, which uses the same 0.9 m cube target used for the results of Figures 3.2 and 3.3. The rough sea surface is for a wind speed of 3 m/s as in Figure 3.1(a), but with different dimensions. This surface is longer in the x-direction because only the $\phi = 0°$ plane of incidence is considered. The target is placed towards the right end of the surface because the incident field is from the left, as shown in Figure 3.13. This longer surface should provide good accuracy for $-87° < \theta < 0°$. The surface is 67x17 wavelengths at a frequency of 1 GHz, and the target is 3 wavelengths. The subtraction approach is again used to extract the target RCS from the total target/surface RCS.

First, to check the accuracy of the finite surface model, Figure 3.14 shows the RCS patterns for a flat surface compared with the same target on an infinite surface. The accuracy

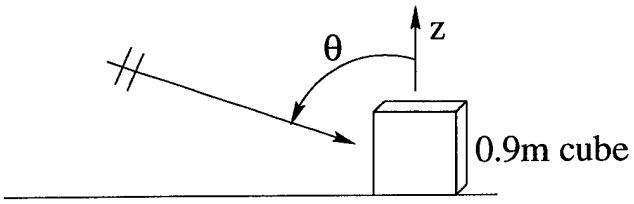

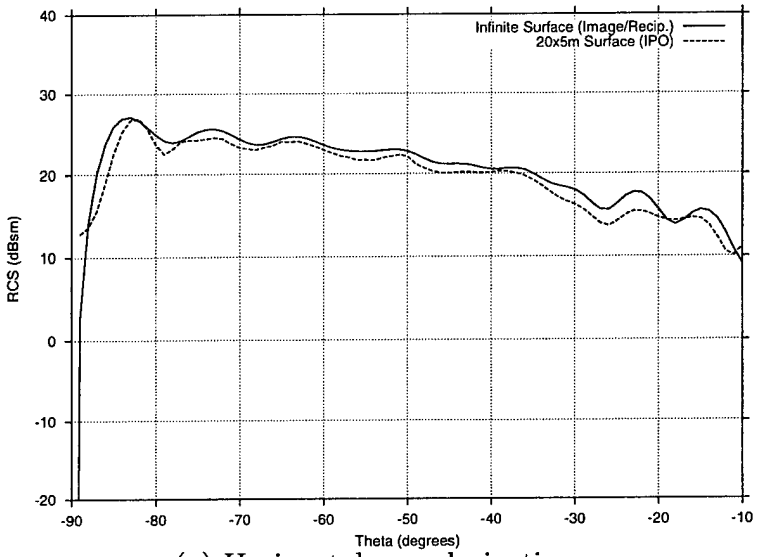

(a) Horizontal co-polarization.

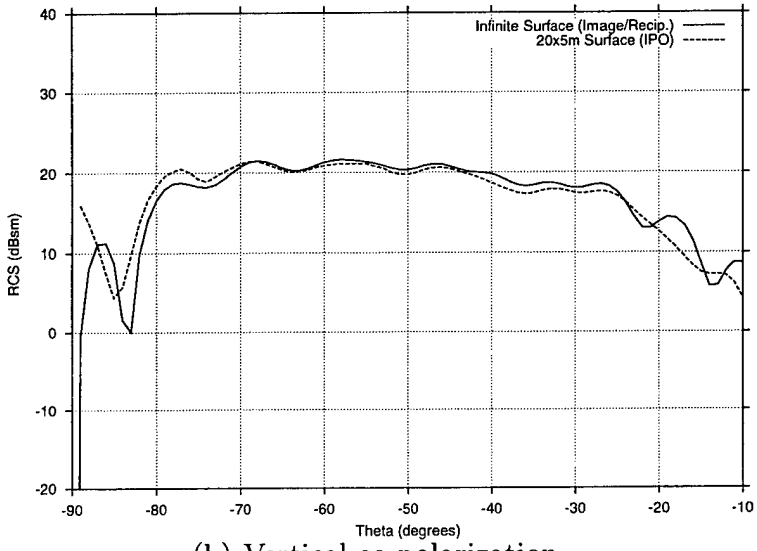

(b) Vertical co-polarization.

Figure 3.14: RCS vs. θ patterns for a 1-block target on a flat sea surface. Frequency = 1 GHz, $\phi = 0°$.

is slightly better than in Figure 3.2, especially for lower elevation angles ($\theta < -81°$) because of the longer surface.

The Monte Carlo simulation uses 6 randomly generated sea surfaces with wind speed 3 m/s. Although this is a relatively small sample size, the mean and variation were verified to converge to within less than a dB over the angular range. Figures 3.15 and 3.16 and show the subtracted RCS data for horizontal and vertical polarization, respectively. It is immediately clear that the co-pol data becomes more random for higher elevation angles, as expected because the incident field is less coherent. However, the cross-pol appears random for all angles.

Figure 3.17 shows the statistical RCS patterns of this data set for the co-polarization case. The average, coherent, incoherent, and maximum RCS curves are shown. As in Chapter 2, these are defined in terms of the far zone scattered electric field $\bar{E}^s$ (with $1/r$ dependence suppressed) as

$$\begin{aligned} \text{Average RCS} &= 4\pi < |\bar{E}^s|^2 > \\ \text{Coherent RCS} &= 4\pi \mid < \bar{E}^s > \mid^2 \\ \text{Incoherent RCS} &= 4\pi \left(< |\bar{E}^s|^2 > - \mid < \bar{E}^s > \mid^2 \right) \\ \text{Maximum RCS} &= 4\pi \max(|\bar{E}^s|^2) \end{aligned} \tag{3.3}$$

where $< \cdot >$ denotes the expected value computed over the entire sample for a given incidence angle. The coherent RCS depends on the phase of the scattered field, so it is always less than or equal to the average RCS which only depends on the magnitude. It is a measure of the time-averaged scattered field at the radar receiver for a target on a time-changing sea surface. The incoherent RCS is a measure of the amount of variation in the RCS for a given angle. The average RCS is the sum of the coherent and incoherent RCS. It is clear from Figure 3.17 that the average RCS is mostly coherent for low elevation angles and incoherent for high elevation angles.

Perhaps the most important curve to the ship designer is the maximum RCS. Clearly the maximum can be considerably higher than the average. Since the sea surface evolves with

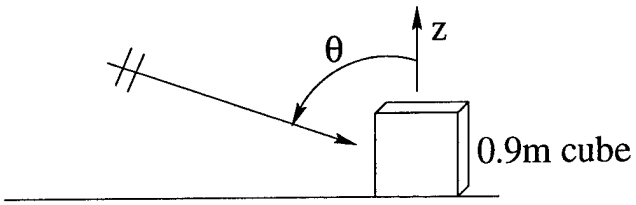

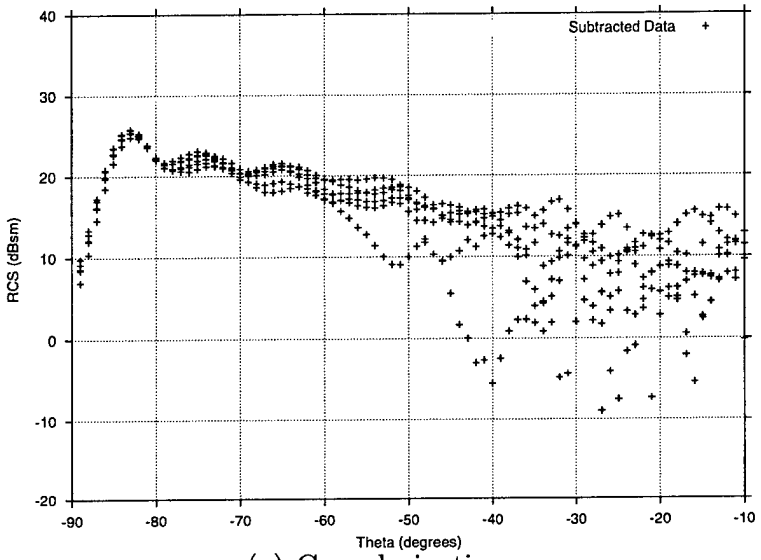

(a) Co-polarization.

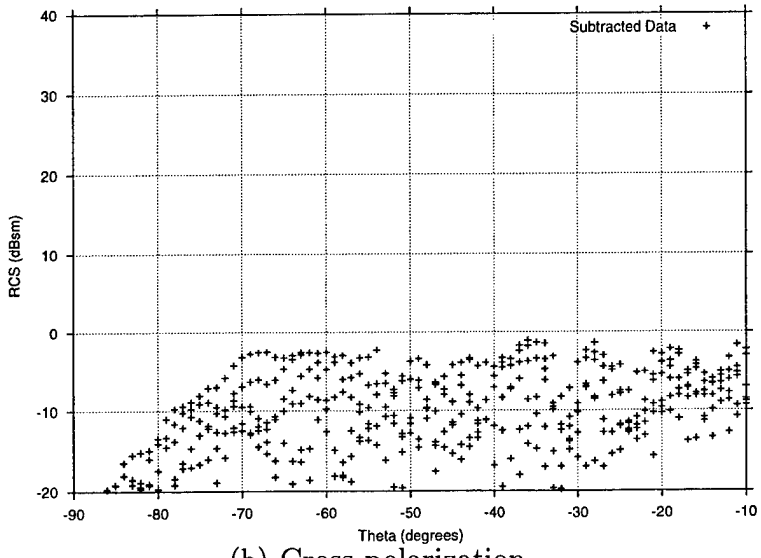

(b) Cross-polarization.

Figure 3.15: RCS vs. θ Monte Carlo data for a 1-block target on 6 randomly generated sea surfaces with wind speed 3 m/s. Incident field is horizontally polarized. Frequency = 1 GHz, $\phi = 0°$.

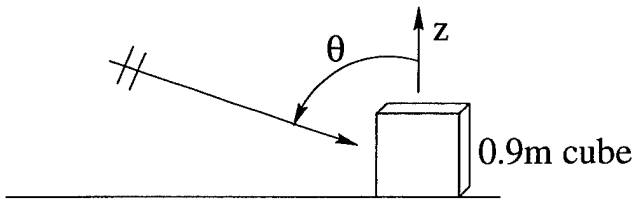

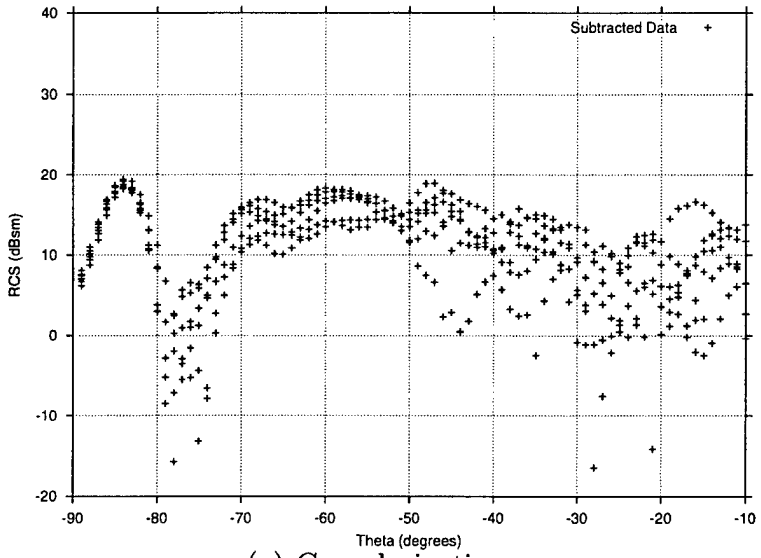

(a) Co-polarization.

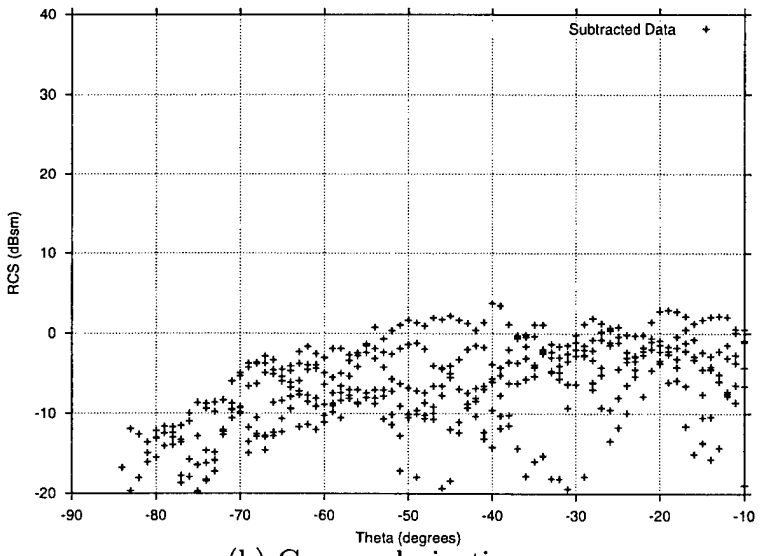

(b) Cross-polarization.

Figure 3.16: RCS vs. θ Monte Carlo data for a 1-block target on 6 randomly generated sea surfaces with wind speed 3 m/s. Incident field is vertically polarized. Frequency = 1 GHz, $\phi = 0°$.

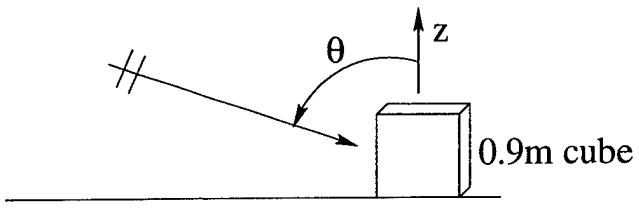

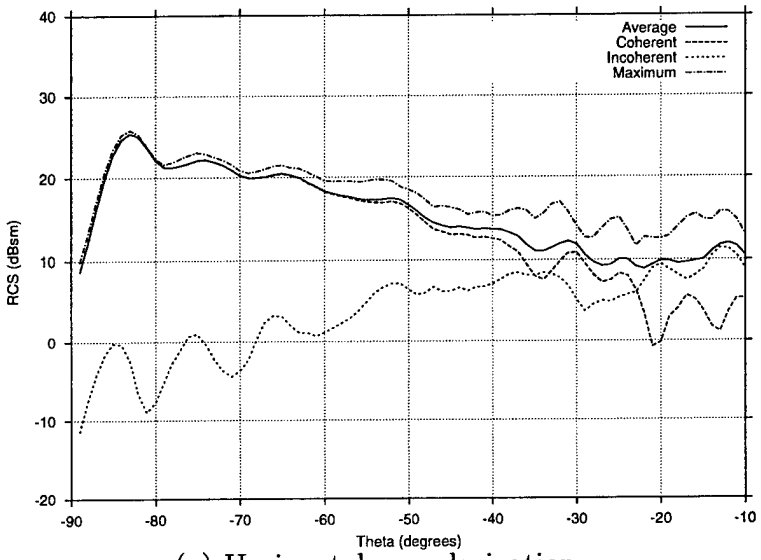

(a) Horizontal co-polarization.

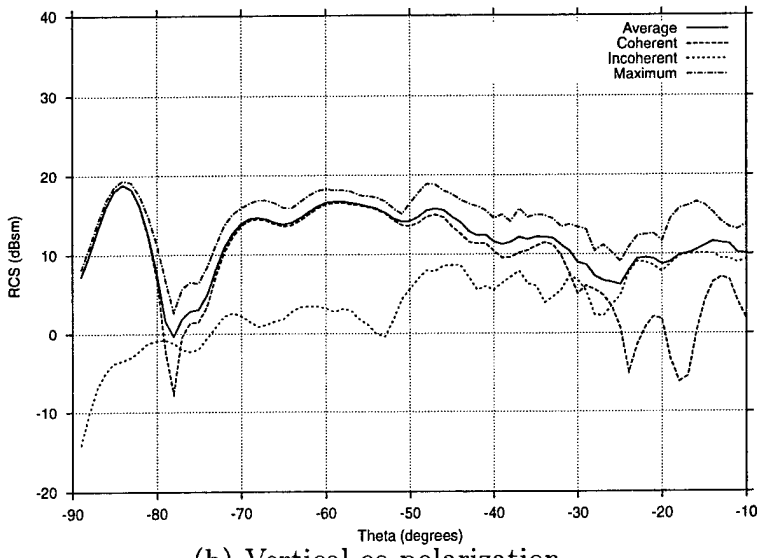

(b) Vertical co-polarization.

Figure 3.17: Statistical RCS vs. θ patterns for a 1-block target on a rough sea surface with wind speed 3 m/s. Frequency = 1 GHz, $\phi = 0°$.

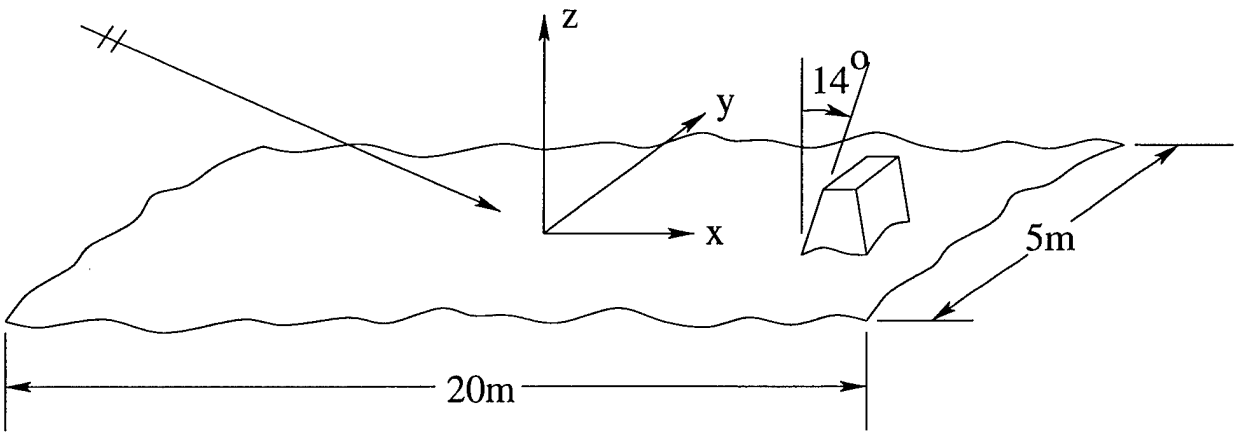

Figure 3.18: 0.9 m low RCS target and surface geometry for the Monte Carlo simulation. Wind speed is 3 m/s.

time much slower than the pulse repitition frequency of a typical radar, peak values of the backscattered field can persist long enough for detection.

3.3.2 Low Cross-Section Target

The same statistial analysis is performed on the lower RCS trapezoidal target shown in Figure 3.18. The base and height of this target are 0.9 m as before, but the sides towards and away from the incident field are tilted inward by 14°. This removes the 90° corner reflector formed by the vertical sides of the block target and the sea surface, and should greatly reduce the RCS for elevation angles lower than 14°. The surface and aspect angles are the same as in the previous case.

The finite surface model is again first validated against the infinite surface in Figure 3.19 for the trapezoidal target. The agreement is very good down to about $-87°$ as before. The RCS levels are generally lower than the block target, except near $\theta = -76°$ which is the angle where the incident field is broadside to the slanted side of the trapezoid.

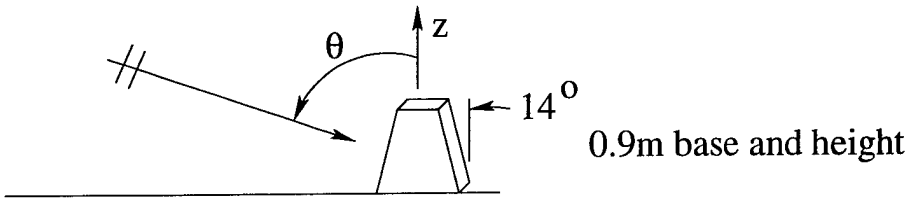

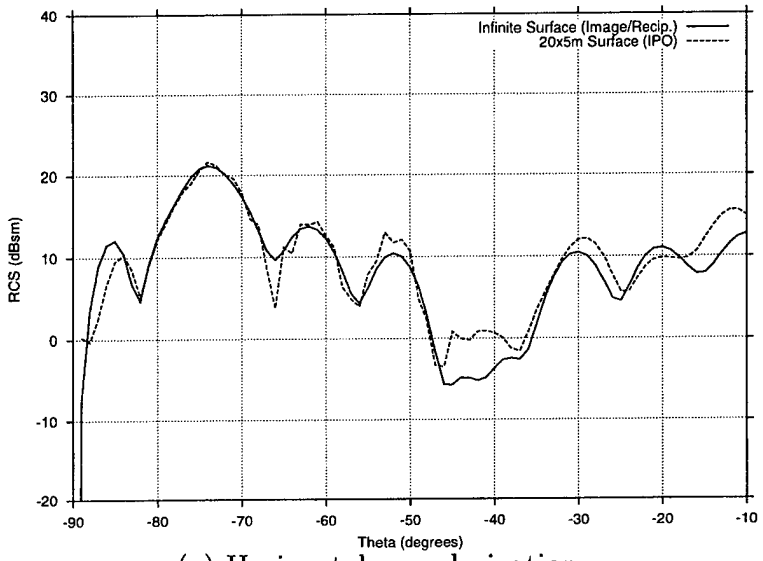

(a) Horizontal co-polarization.

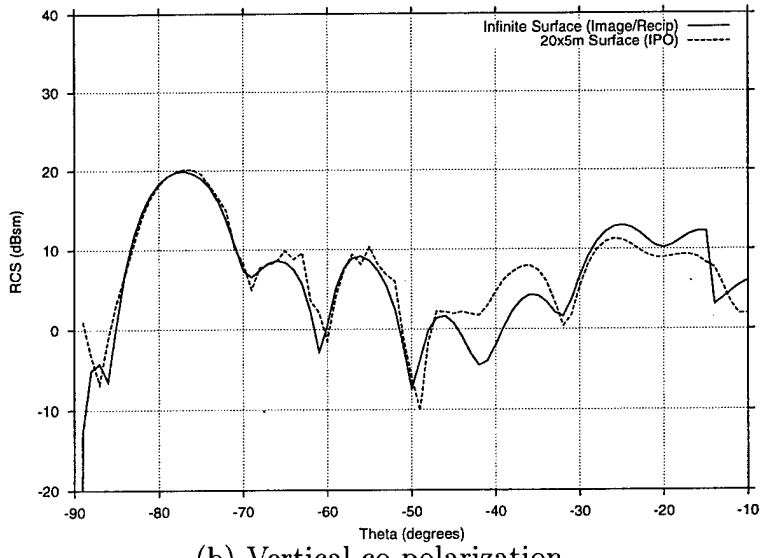

(b) Vertical co-polarization.

Figure 3.19: RCS vs. θ patterns for a trapezoidal target on a flat sea surface. Frequency = 1 GHz, $\phi = 0°$.

Figures 3.20 and 3.21 show the complete set of subtracted RCS data for the trapezoid for 6 randomly generated sea surfaces with wind speed 3 m/s. The behavior is basically similar to the block target, i.e., the co-pol data becomes more random for higher elevation angles and the cross-pol data is random everywhere. However, it does appear that the trapezoidal co-pol data tends to become random at a lower elevation angle than for the block target.

Figure 3.22 shows the average, coherent, incoherent and maximum RCS curves for the Monte Carlo simulation of the trapezoidal target. As with the block target, the average RCS is mostly coherent for low elevation angles and incoherent for large elevation angles. But as the raw data plots suggested, the average RCS becomes incoherent at a lower elevation angle than for the block target. In the next section the statistical data for both targets is compared with a variety of ray-optical computational approaches based on a locally flat surface.

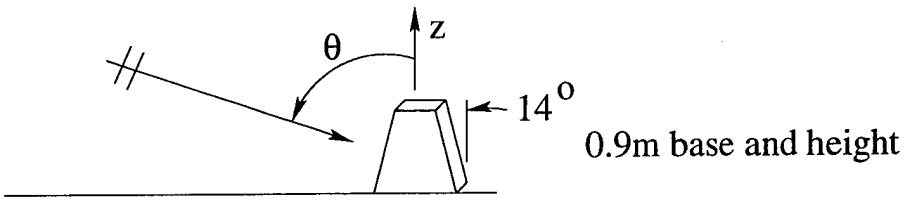

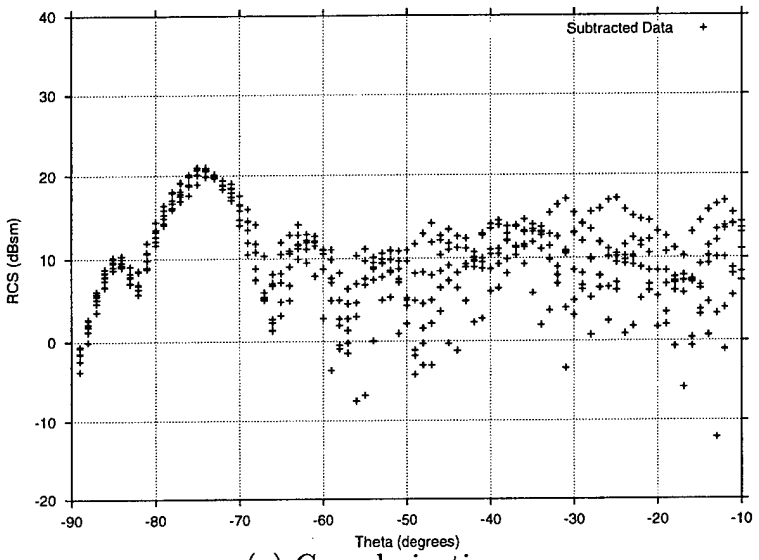

(a) Co-polarization.

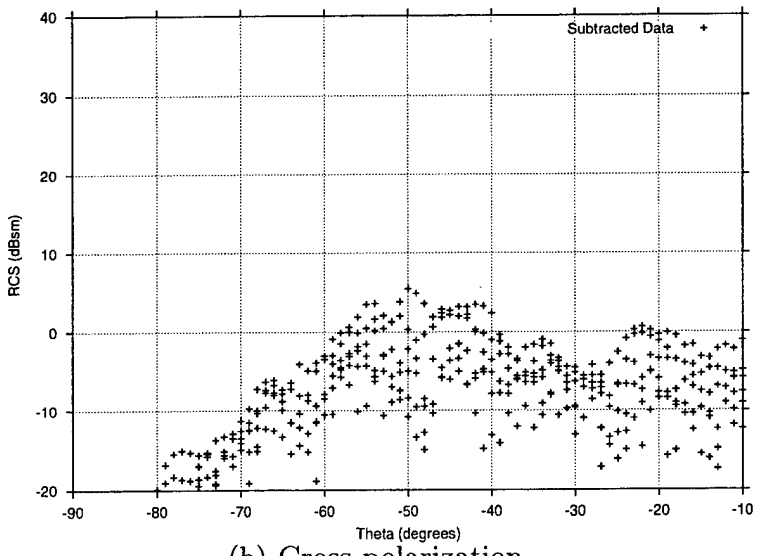

(b) Cross-polarization.

Figure 3.20: RCS vs. θ Monte Carlo data for a trapezoidal target on 6 randomly generated sea surfaces with wind speed 3 m/s. Incident field is horizontally polarized. Frequency = 1 GHz, $\phi = 0°$.

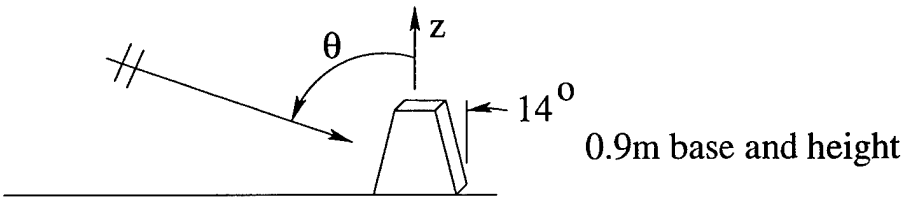

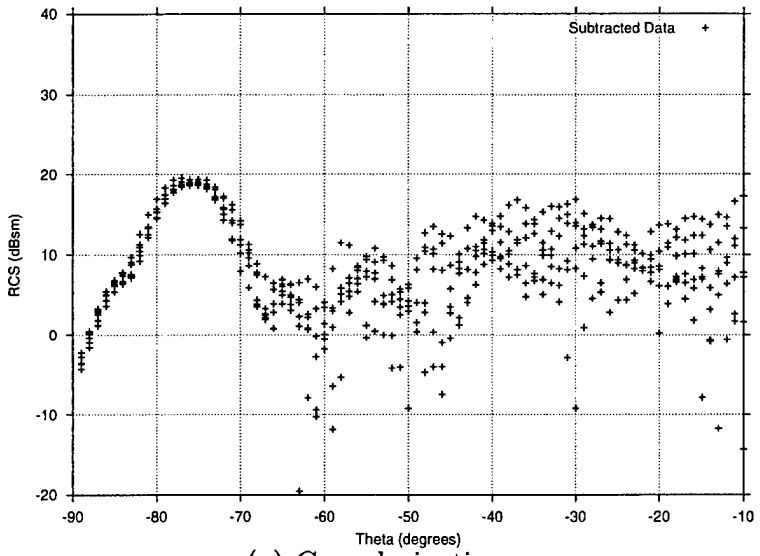

(a) Co-polarization.

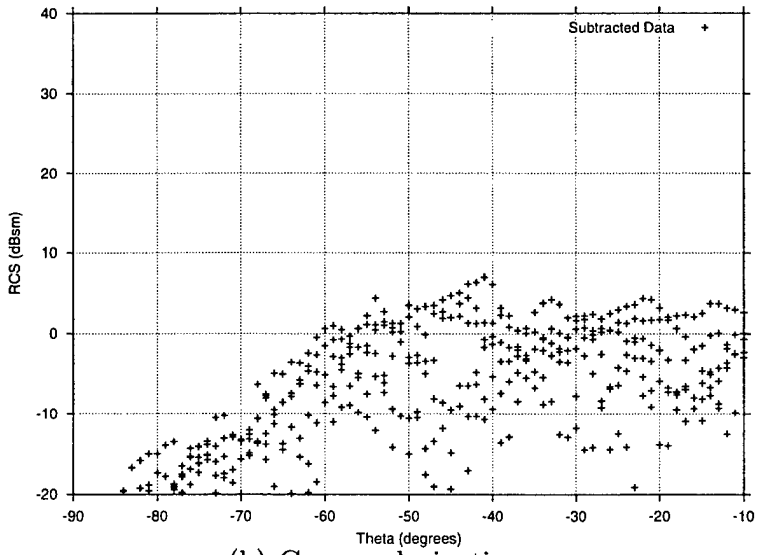

(b) Cross-polarization.

Figure 3.21: RCS vs. θ Monte Carlo data for a trapezoidal target on 6 randomly generated sea surfaces with wind speed 3 m/s. Incident field is vertically polarized. Frequency = 1 GHz, $\phi = 0°$.

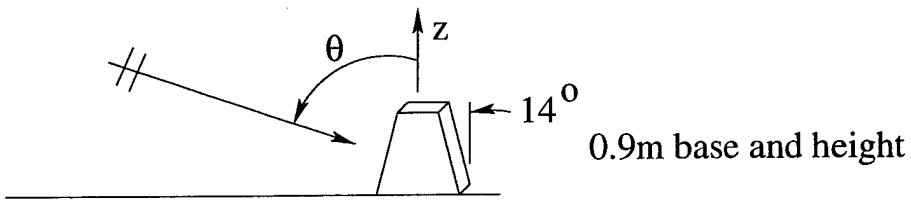

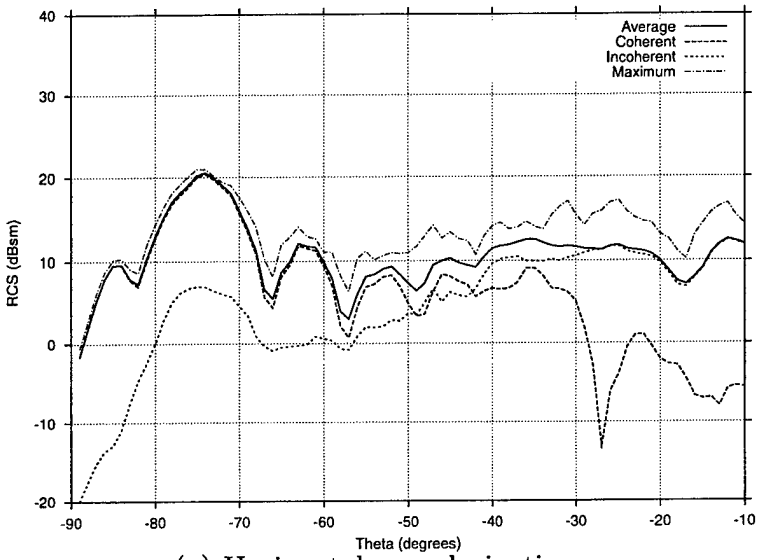

(a) Horizontal co-polarization.

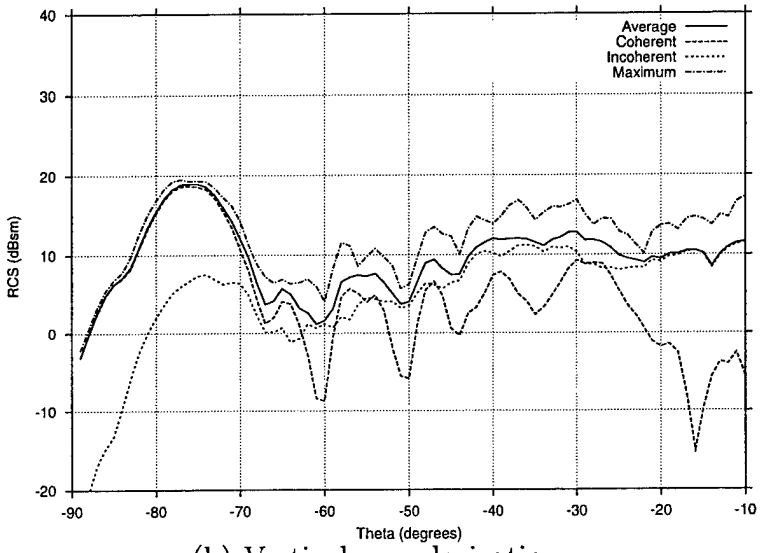

(b) Vertical co-polarization.

Figure 3.22: Statistical RCS vs. θ patterns for a trapezoidal target on a rough sea surface with wind speed 3 m/s. Frequency = 1 GHz, $\phi = 0°$.

3.4 Plane Wave Approaches

As discussed in the Chapter 1, one of the primary goals of this research project is to develop ray-optical approaches for computing the scattering from targets on a rough sea surface. Since realistic targets are hundreds or thousands of wavelengths in size at radar frequencies, and the portion of the sea surface which would have to be included in the model is even larger, numerical methods are completely intractable. It is therefore of interest to use a plane wave characterization of the reflection from the sea surface so that a large randomly generated rough surface does not need to be included in the model. Furthermore, existing RCS predictions codes may be used with little modification. In this section some plane wave approaches are considered.

3.4.1 Flat Surface and Coherent Plane Wave Computations

The simplest approach is to compute the RCS patterns of a given target on a flat sea surface. Figure 3.23 shows the statistical RCS patterns of the block target of Figure 3.13 compared with the infinite flat surface result. The flat surface RCS is higher than the average and maximum RCS of the 3 m/s rough surface everywhere except for some high elevation angles, and for the Brewster angular region for V-pol. If it were not for the unexplained Brewster angle effect, it would be reasonably safe to assume the flat surface RCS predicts the maximum RCS level for this target.

Figure 3.24 shows the same patterns for the low RCS trapezoidal target of Figure 3.18. Here it is clear that the flat surface RCS may be considerably lower than the rough surface RCS. Therefore, it cannot be assumed that the flat surface RCS is always higher than the rough surface RCS. Also, the Brewster angle effect for V-pol is not as noticable for the trapezoidal target as for the block target, although there is still a discrepancy for low elevation angles.

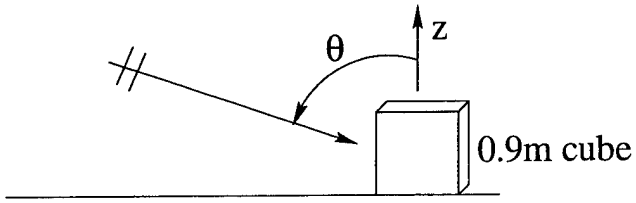

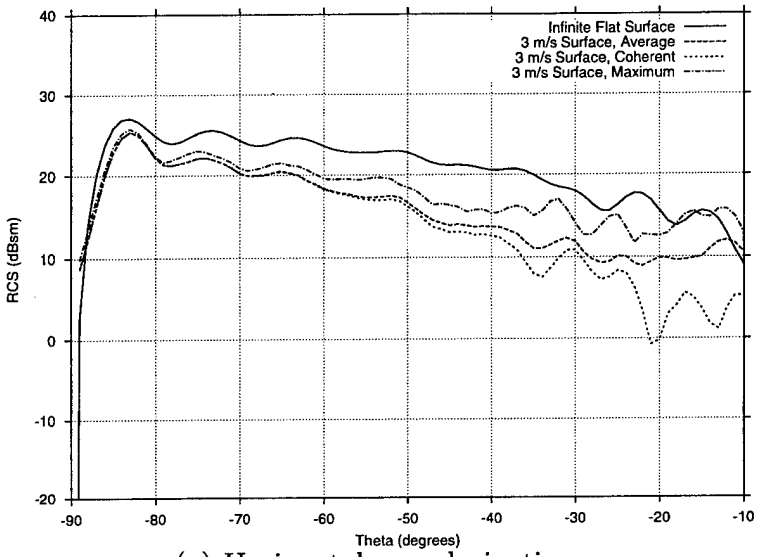

(a) Horizontal co-polarization.

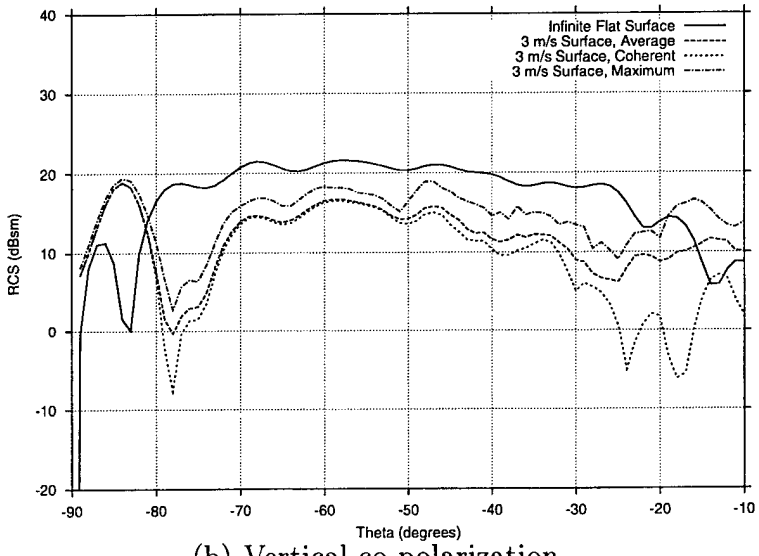

(b) Vertical co-polarization.

Figure 3.23: Statistical RCS vs. θ patterns for a 1-block target on a rough sea surface with wind speed 3 m/s compared with infinite flat surface result. Frequency = 1 GHz, $\phi = 0°$.

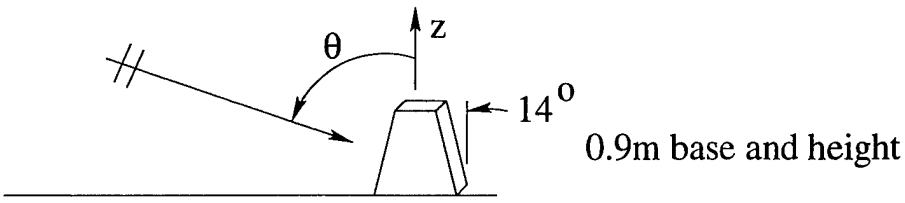

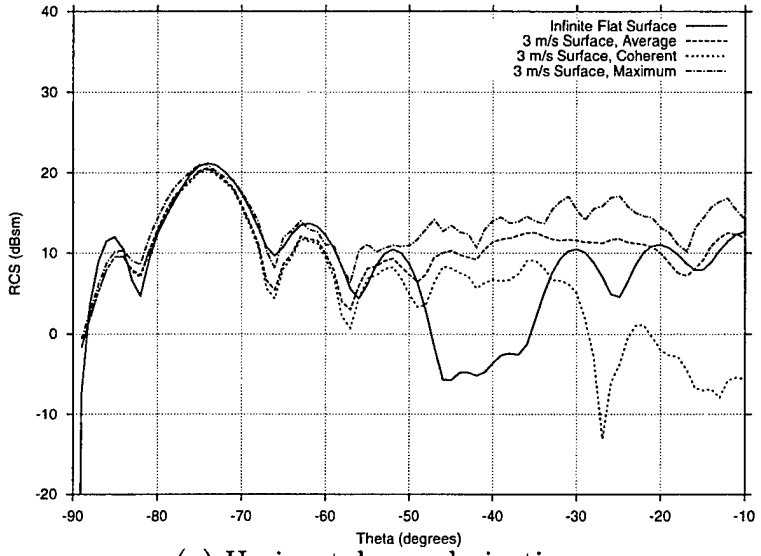

(a) Horizontal co-polarization.

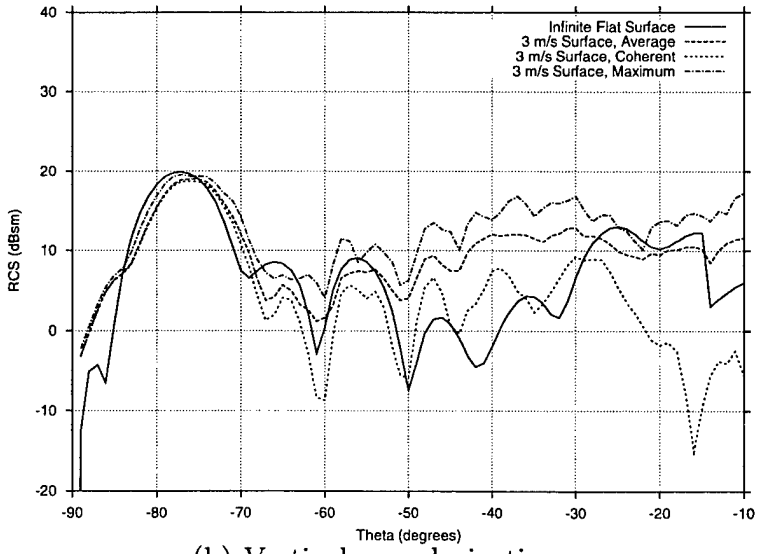

(b) Vertical co-polarization.

Figure 3.24: Statistical RCS vs. θ patterns for a trapezoidal target on a rough sea surface with wind speed 3 m/s compared with infinite flat surface result. Frequency = 1 GHz, $\phi = 0°$.

As discussed for 2D problems in Chapter 2, another possible plane wave approach is to weight the sea reflected incident field by the coherent plane wave reflection coefficient of (2.4). For a given wind speed and elevation angle, the reflection off the sea surface will be reduced by this factor. It may be expected that the RCS of the target computed using this coherent incident field will approximate the coherent RCS. Figure 3.25 shows the RCS patterns computed in this manner compared with the statistical results for the block target. The infinite surface coherent results is a reasonable approximation for the coherent RCS for H-pol, but is very bad for V-pol because of the Brewster angle region.

Figure 3.26 shows the same result for the low RCS trapezoidal target. It is clear that the infinite surface coherent RCS is a poor approximation for the actual coherent RCS, except for low elevation angles when the RCS is dominated by the coherent component (i.e., $\Gamma \approx 1$). Furthermore, as mentioned in the 2D results, the coherent reflected field approach is not advisable because the incident and reflected plane waves do not satisfy the boundary condition at the sea surface interface. This could give rise to non-physical scattering mechanisms.

The previous results have shown that the infinite flat surface plane wave approaches are only reliable for low elevation angles when the incident field is highly coherent ($\Gamma \approx 1$). The exception is the V-pol case in the Brewster angle region, which is not currently understood. When the incident field is less coherent, the plane wave approaches may greatly underpredict the average and maximum RCS levels.

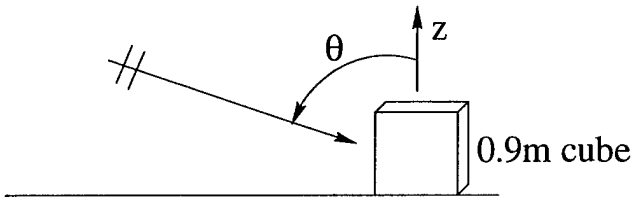

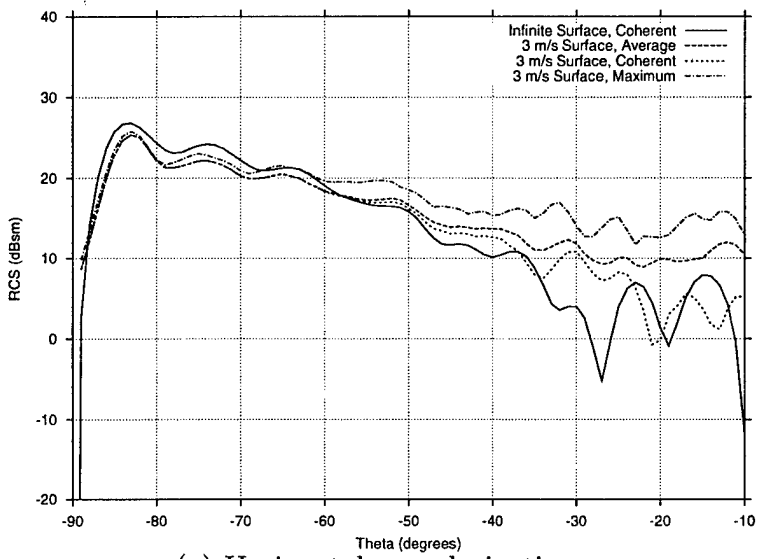

(a) Horizontal co-polarization.

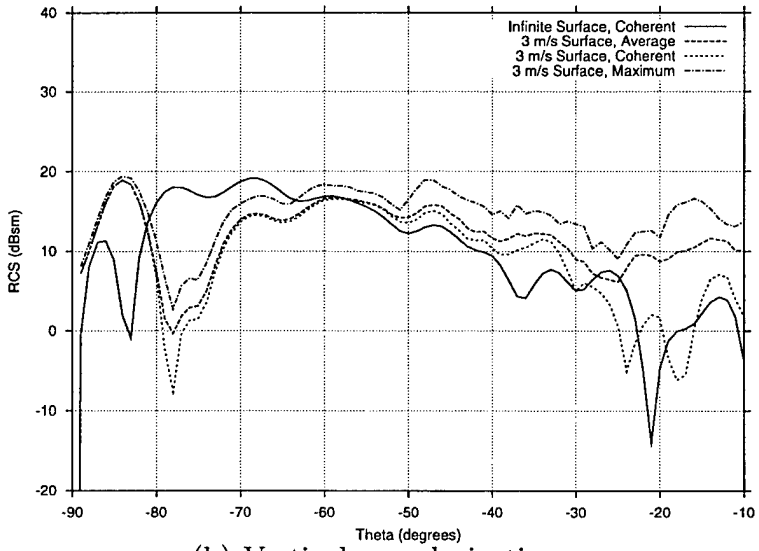

(b) Vertical co-polarization.

Figure 3.25: Statistical RCS vs. θ patterns for a 1-block target on a rough sea surface with wind speed 3 m/s compared with infinite flat surface coherent result. Frequency = 1 GHz, $\phi = 0°$.

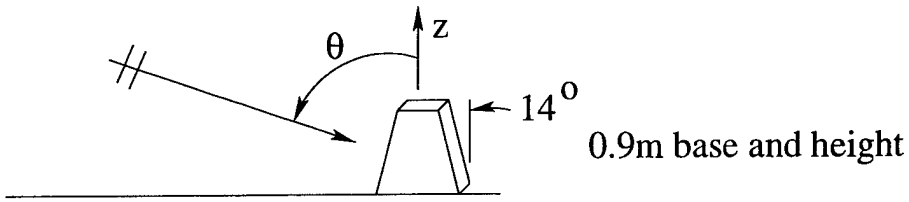

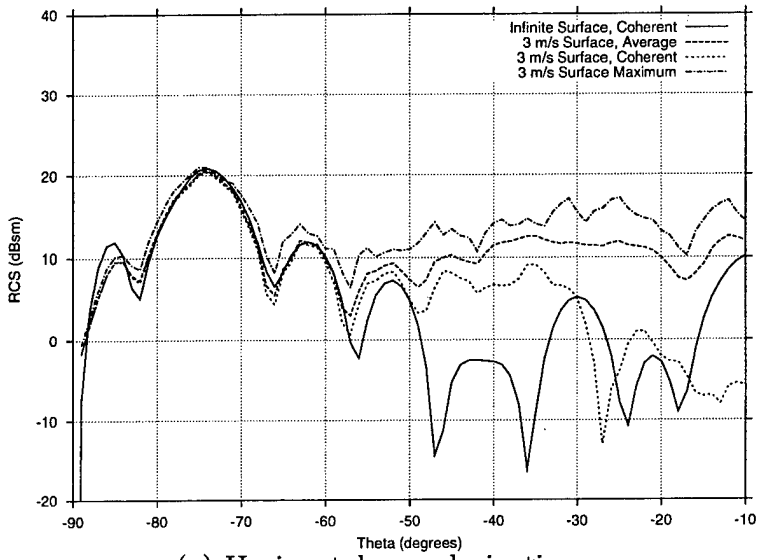

(a) Horizontal co-polarization.

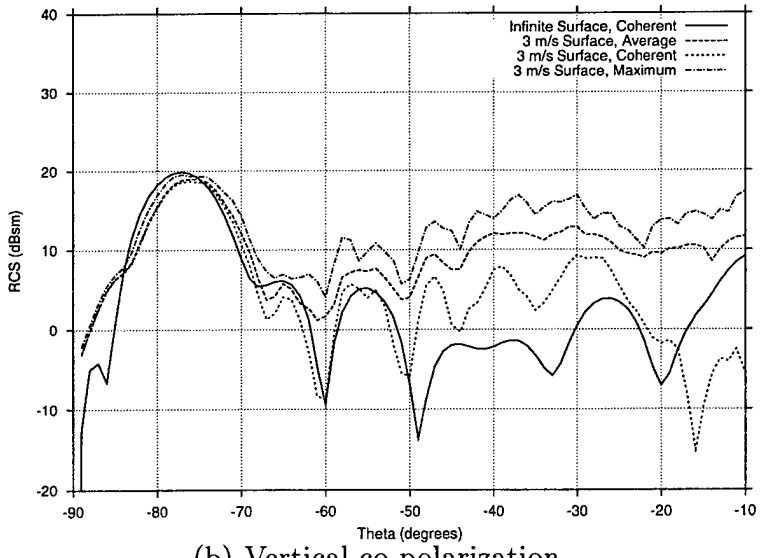

(b) Vertical co-polarization.

Figure 3.26: Statistical RCS vs. θ patterns for a 1-block target on a rough sea surface with wind speed 3 m/s compared with infinite flat surface coherent result. Frequency = 1 GHz, $\phi = 0°$.

3.4.2 Tilted Plane (Roll Angle) Computation

It has been suggested in the 2D studies that the tilted plane model, or equivalently, the RCS vs. roll angle plot, may give a better indication of the amount of expected variation in the RCS. Figures 3.27(a) and (b) show the roll angle plots for the block and trapezoidal targets, respectively, on an infinite flat surface for an incidence angle of $\theta = -40°$.

Looking at Figure 3.23, it is seen that there is about a 7-9 dB difference between the flat surface RCS and the average RCS at an incidence angle of $\theta = -40°$ for the block target. This is approximately the range of variation of the RCS in the roll angle plot. Likewise, Figure 3.24 shows a 12-15 dB difference between the flat surface RCS and the average RCS at $\theta = -40°$ for the trapezoidal target, and that the flat surface RCS is much lower than the average rough surface RCS. The roll angle plot for the trapezoid shows a minima for zero roll angle, and a large range of variation in the RCS. Therefore, the roll angle plots tend to explain the amount of variation in the RCS for the same targets on a rough surface.

What remains to be determined is how the wind speed affects the maximum roll angle. Comparing Figure 3.27 with the Maximum RCS curves of Figures 3.23 and 3.24, it appears that a maximum roll angle of about 5° is sufficient for a wind speed of 3 m/s. Ideally, it would be of interest to determine the maximum roll angle from the average slope of the long waves in the ocean spectrum and the rolling of a ship for a given sea state. As an initial approximation, the average slope is assumed to be the RMS wave height $\hat{\sigma}$ divided by one-half the longest wavelength included in the ocean spectrum. For a 3 m/s wind speed the low frequency cut-off wavelength in the power law spectrum is 1.09 m and the RMS wave height is 0.0486 m. This corresponds to a tilted plane rotation angle of 5.1°, which is very close to our estimate of the roll angle range of interest. This result further supports the utility of the tilted plane model.

It should be mentioned again that the variation of the RCS as a function of roll angle is highly target dependent. In Chapter 2 of [2] it was shown that the roll angle plot for a 2D ship with a vertical hull showed large variations around 0° roll angle. This is due to the strong corner reflector scattering when the hull makes an angle of 90° with the sea surface,

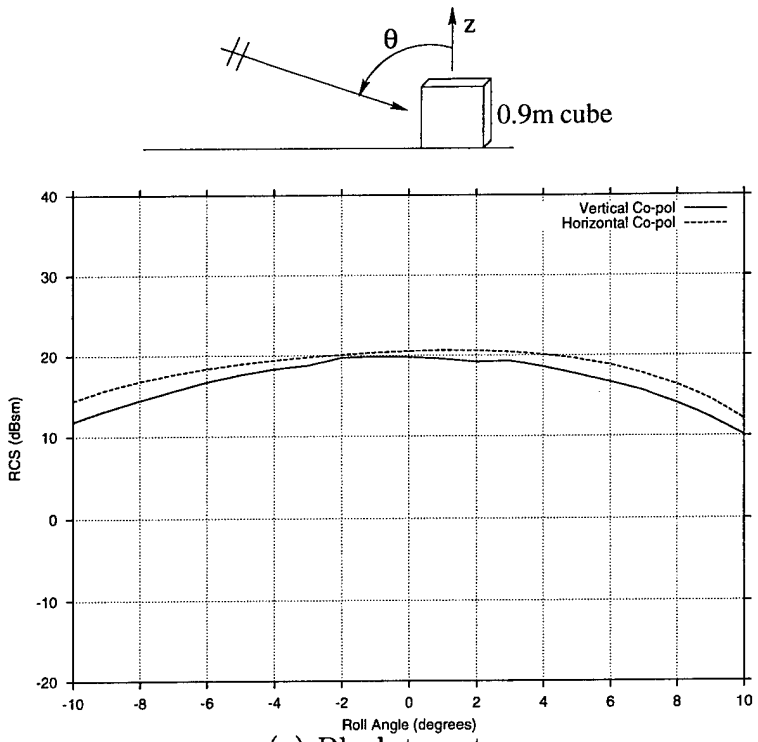

(a) Block target.

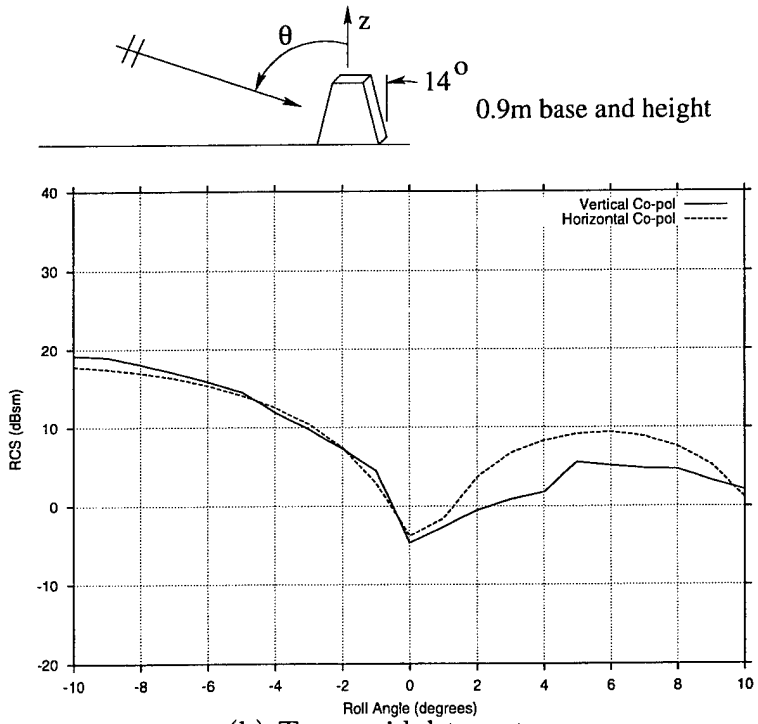

(b) Trapezoidal target.

Figure 3.27: RCS vs. roll angle patterns for the block and trapezoidal targets on an infinite flat surface. Frequency = 1 GHz, $\theta = -40°$, $\phi = 0°$.

which rapidly drops off as the ship rolls. This is true even for a very low grazing angle when the incident field is highly coherent. Whether the variation is caused by the rough surface or the rolling of the target, the roll angle plot appears to predict the maximum variation in the RCS.

Chapter 4

Scattering Over a Spherical Earth

4.1 Introduction

This chapter presents some numerical results which demonstrate the effect of Earth curvature on the scattering from a 3D target. First, Section 4.2 presents some additional computations of the incident field over a spherical earth. In [1] and [2] only horizontal polarization was considered. The new results include vertical polarization, which models the sea surface with an impedance boundary condition. Rough surface results are also included which were computed using the parabolic wave method. Section 4.3 presents numerical results for the scattering from a 3D target on a spherical earth sea surface compared with a target on a flat surface, and demonstrates how the scattering decreases as a function of range, especially as the target moves beyond the horizon.

As mentioned several times throughout this study, a ray-optical model for the incident field is required so that conventional RCS prediction codes can be used. Figure 4.1 shows the pertinent rays for a target on a spherical earth. For points above the line-of-sight (LOS) horizon the incident field is composed of a direct and reflected ray. For points below the LOS horizon the incident field is a creeping ray which attaches to the surface at the horizon, creeps along the surface to the detachment point, and sheds away from the surface to the field point. If the target is located before the attachment point at the horizon, then the incident field is only the incident and reflected rays. If the target is located completely beyond the LOS horizon, then the incident field is only the creeping wave. The angles of

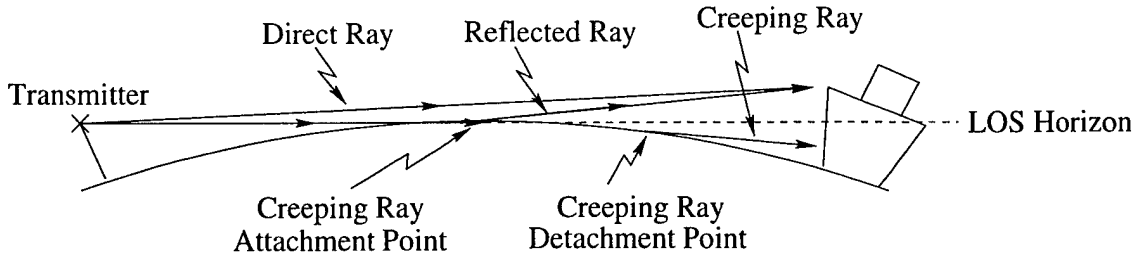

Figure 4.1: Ray-optical model for the incident fields illuminating a target on a spherical earth.

incidence of each ray can be found from trigonometry. The reflected ray obeys Snell's law of reflection, and the creeping ray is defined as the shortest path between the transmitter and reciever when the reciever is shadowed by the earth. The creeping ray is tangent to the earth's surface at the attachment and detachment points.

4.2 Incident Field Over a Spherical Earth Sea Surface

The incident fields over a smooth spherical earth are generated using the Fock solution, which is a rapidly convergent series of Airy functions [15, 16]. The solution is based on the eigenfunction expansion for a sphere, so it is asymptotically exact. It is most efficient when the receiver is in the shadow region beyond the LOS horizon, or close to it. Otherwise, when the observer is in the lit region away from the LOS horizon, the geometrical optics solution is valid.

Figure 4.2 shows the Fock solution for the incident fields over a spherical earth as a function of receiver height, for ranges before and after the horizon. A linear refractivity profile of the atmosphere is taken into account by adjusting the curvature of the earth by a factor of 4/3. The field strength is normalized to free space propagation. It is noted that the fields appear to be the interference pattern of an incident and reflected ray before the horizon, whereas they are evanescent close to the surface for the over-the-horizon case (20 km). It is also noted that the vertically polarized fields are slightly lower than for horizontal polarization.

The parabolic wave equation (PWE) method is also used so that surface roughness can be

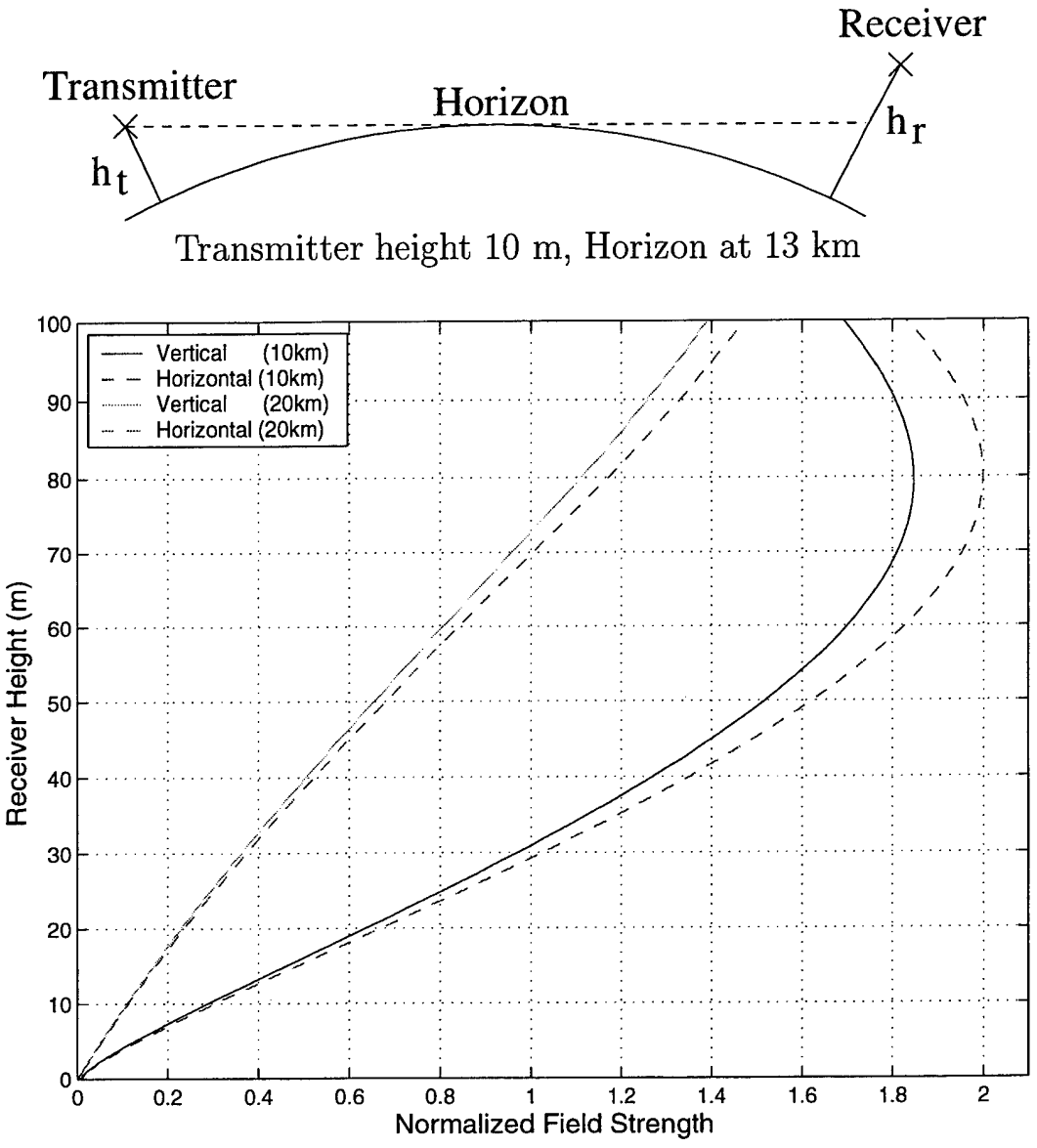

Figure 4.2: Fock Airy function solution for the normalized electric field vs. receiver height over a spherical earth sea surface. Frequency = 1 GHz.

included in the results [17, 18]. In the PWE method, the PWE is solved step-wise at a series of cross-sections along the propagation path from source to receiver. As an approximate numerical solution, its accuracy degrades as the propagation distance increases. The PWE solution is in 2D, but the curvature of the earth is accounted for and the fields are normalized to free space propagation, so it is possible to compare the PWE results with the 3D Fock results. The Advanced Propagation Model (APM) code is used to generate the PWE results [19].

Figures 4.3 and 4.4 show the fields over a rough sea surface computed using the PWE method for ranges of 10 km and 20 km, respectively. The results for 3 random rough surface realizations with wind speed 15 m/s are shown. As expected, the 3 curves tend to be more random for higher receiver heights, and converge close to the surface. For these cases the horizontal and vertical polarizations appear to be very similar.

Figures 4.5 and 4.6 compare the PWE solutions (PE) with the ray-optical solutions (RO) for wind speeds of 5 m/s and 15 m/s, respectively. The "RO (smooth)" case is the ray-optical solution for a smooth earth surface, and the "RO" case is the ray-optical solution for the coherent field over a rough earth surface, computed using the coherent reflection coefficient of (2.4). The 5 m/s case shows that all 3 curves are very similar, so the field is highly coherent and the rough surface has little effect. The 15 m/s case shows that even though the ray-optical field is highly coherent up to a receiver height of 70 m, the PWE solution is somewhat lower in magnitude and the peak is shifted. This suggests that the coherent reflection coefficient may over-estimate the coherent component of the incident field for very rough surfaces. Further investigation is required to resolve this question.

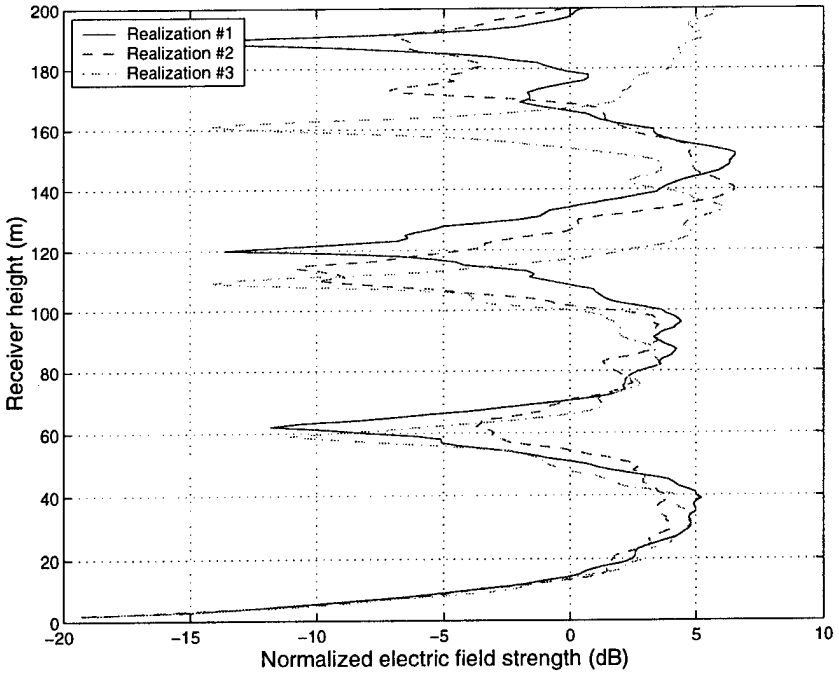

(a) Horizontal polarization.

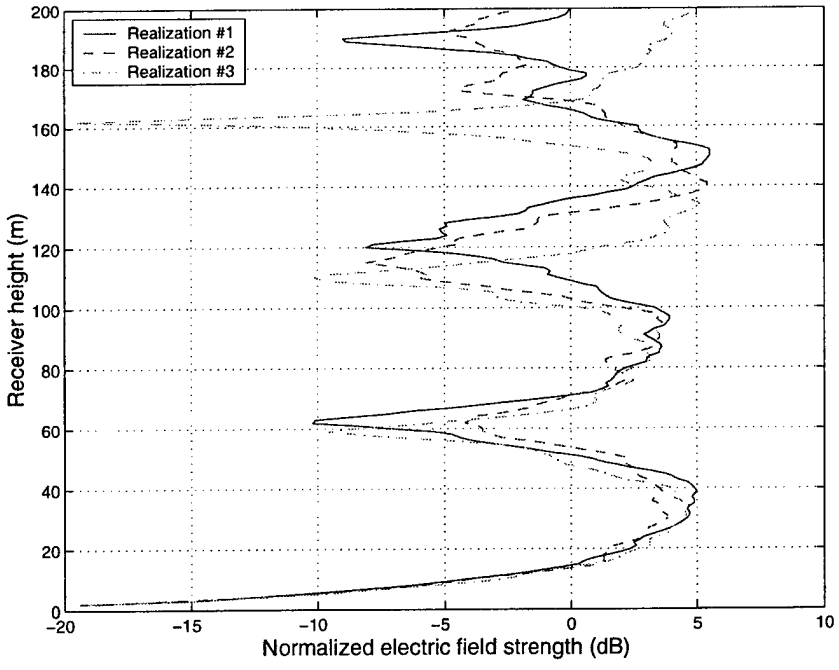

(b) Vertical polarization.

Figure 4.3: Normalized incident electric field vs. reciever height over a spherical earth rough sea surface. Computed using PWE method for 3 surface realizations with wind speed 15 m/s. Frequency = 3 GHz, transmitter height = 10 m, range = 10 km, horizon at 13 km.

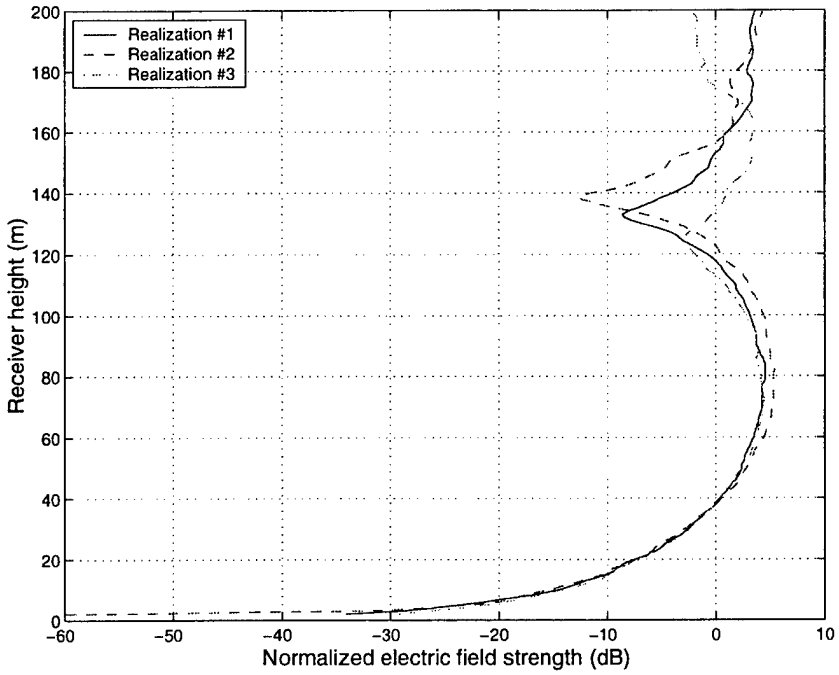

(a) Horizontal polarization.

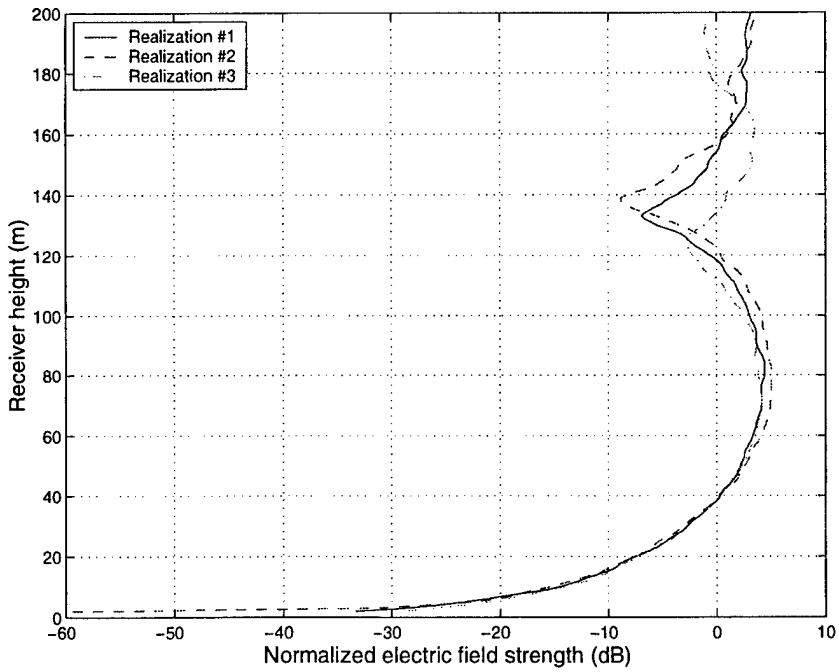

(b) Vertical polarization.

Figure 4.4: Normalized incident electric field vs. reciever height over a spherical earth rough sea surface. Computed using PWE method for 3 surface realizations with wind speed 15 m/s. Frequency = 3 GHz, transmitter height = 10 m, range = 20 km, horizon at 13 km.

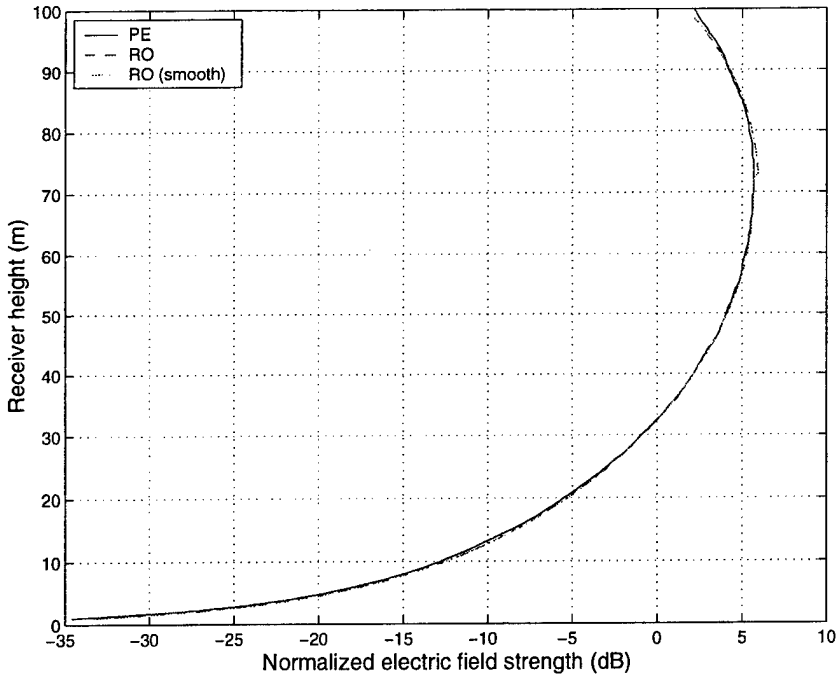

(a) Horizontal polarization.

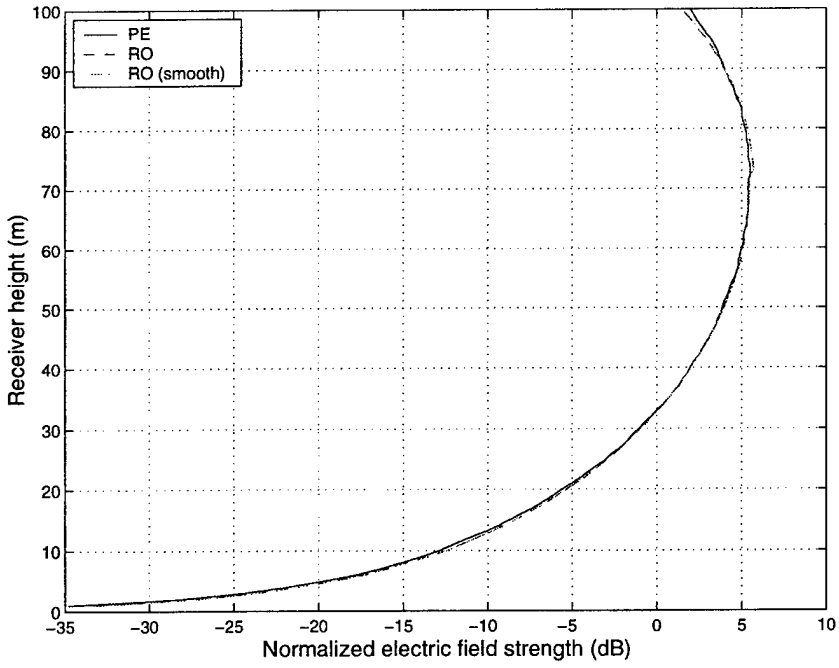

(b) Vertical polarization.

Figure 4.5: Normalized incident electric field vs. reciever height over a spherical earth rough sea surface. Computed using PWE method (PE) with wind speed 5 m/s, and ray-optical (RO) solutions. Frequency = 3 GHz, transmitter height = 10 m, range = 20 km, horizon at 13 km.

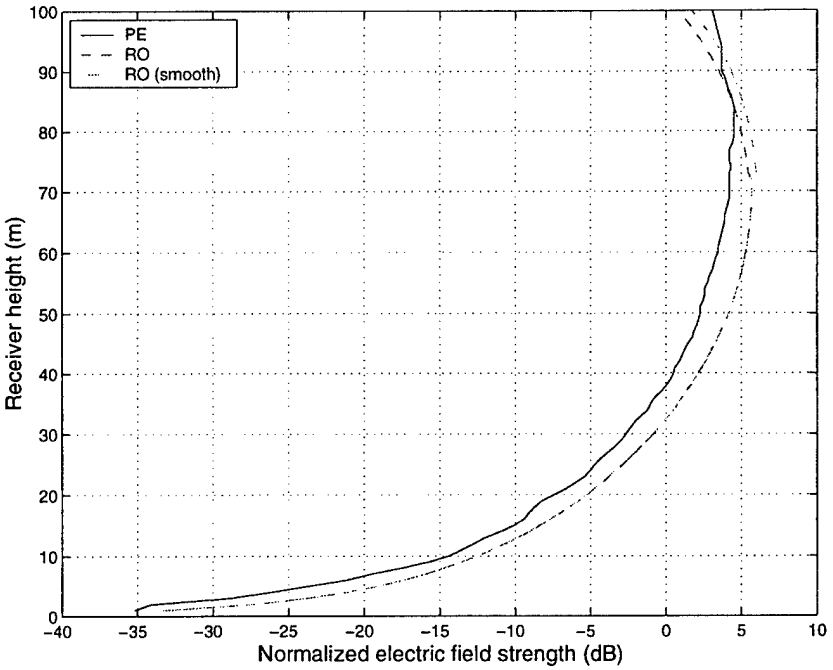

(a) Horizontal polarization.

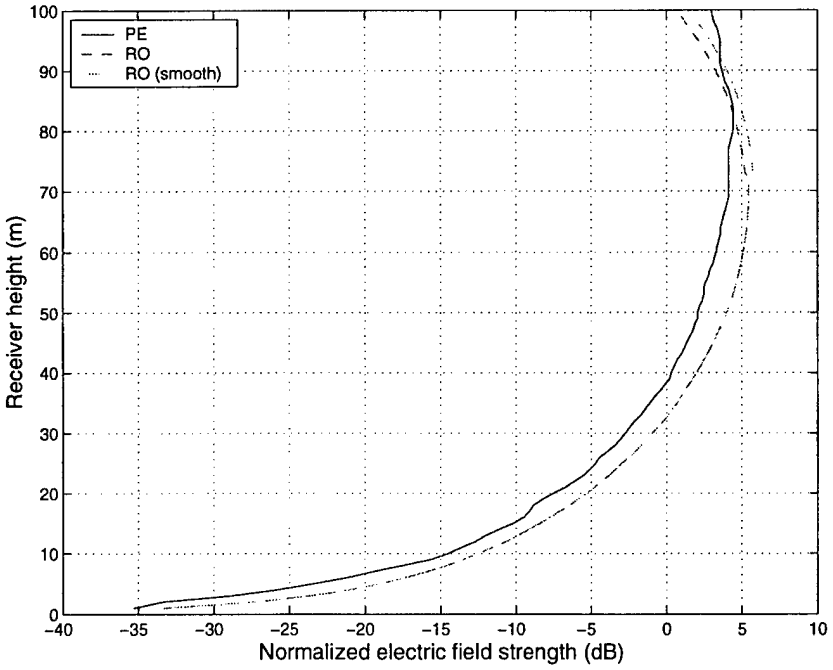

(b) Vertical polarization.

Figure 4.6: Normalized incident electric field vs. reciever height over a spherical earth rough sea surface. Computed using PWE method (PE) with wind speed 15 m/s, and ray-optical (RO) solutions. Frequency = 3 GHz, transmitter height = 10 m, range = 20 km, horizon at 13 km.

4.3 Scattering from a 3D Target on a Spherical Earth Sea Surface

The numerical results of this section were generated using the Fock solution for the incident fields over a spherical earth as discussed in the previous section. Figure 4.7 plots the incident electric field as a function of range for a receiving point which is 1 m above the sea surface. The field is normalized to free space propagation. The transmitter height is 10 m and the frequency is 1 GHz. This is the incident field used in the RCS results of this section. Also shown is the incident field over a flat earth. As expected, the fields over a spherical earth drop rapidly beyond the horizon. It is also noted that the vertically polarized fields are about 1 dB lower than horizontal for this case.

In the following RCS results the incident field is generated by a vertically or horizontally oriented point dipole source located at the transmitter. Technically, the RCS is defined relative to an incident plane wave. However, since it is not possible to define an incident plane wave for this scenario, the RCS is defined relative to the free space incident field of the dipole. Physical optics is used to compute the scattered fields over the target, and the reciprocity integral is used to compute the backscattered fields at the source.

Figure 4.8 shows the RCS of a 3D block target on a spherical earth sea surface as a function of range. The target is the same 0.9 m cube used in Chapter 3. The transmitter height is 10 m, and the horizon is located at range 13 km. Also shown is the RCS computed with the target on a flat surface for comparison. As expected, the spherical earth RCS results drop significantly as the target moves beyond the horizon. It is also noted that the RCS is about 4 dB lower for vertical polarization than for horizontal. This is not expected considering that the vertically polarized incident field of Figure 4.7 is only about 1 dB lower than horizontal. It may be possible that the RCS difference is target and/or frequency dependent. For both polarizations the RCS drops faster than the incident field as the target moves farther over the horizon, but this is due to the fact that the received radar scattering signal undergoes a two-way propagation path to and from the target.

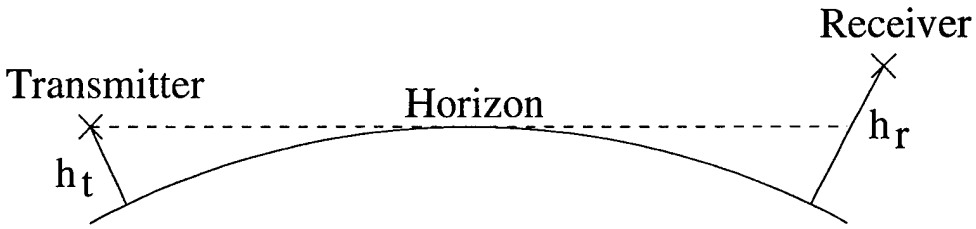

Transmitter height 10 m, Receiver height 1 m, Horizon at 13 km

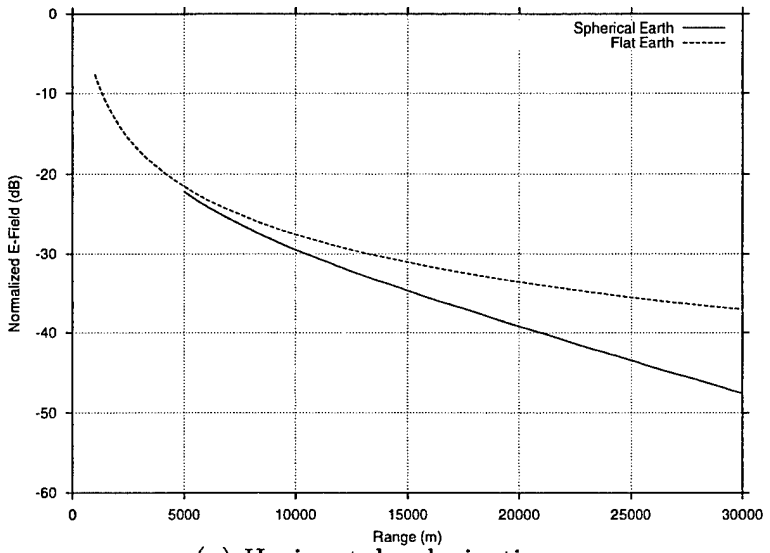

(a) Horizontal polarization.

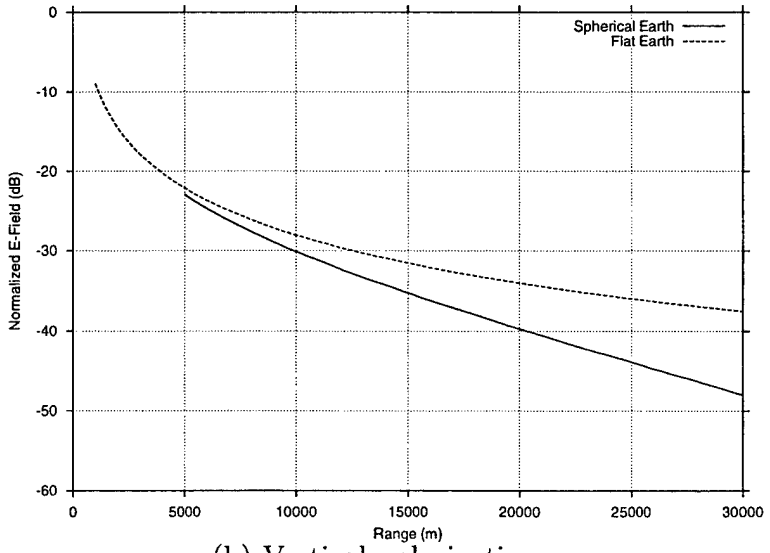

(b) Vertical polarization.

Figure 4.7: Normalized incident electric field vs. range for a point 1 m above a spherical and flat earth. Frequency = 1 GHz.

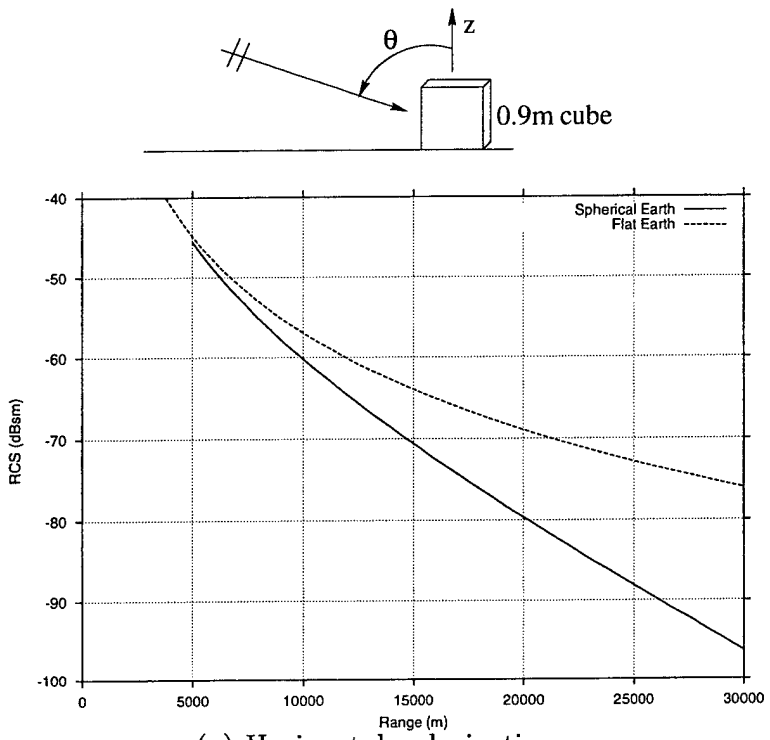

(a) Horizontal polarization.

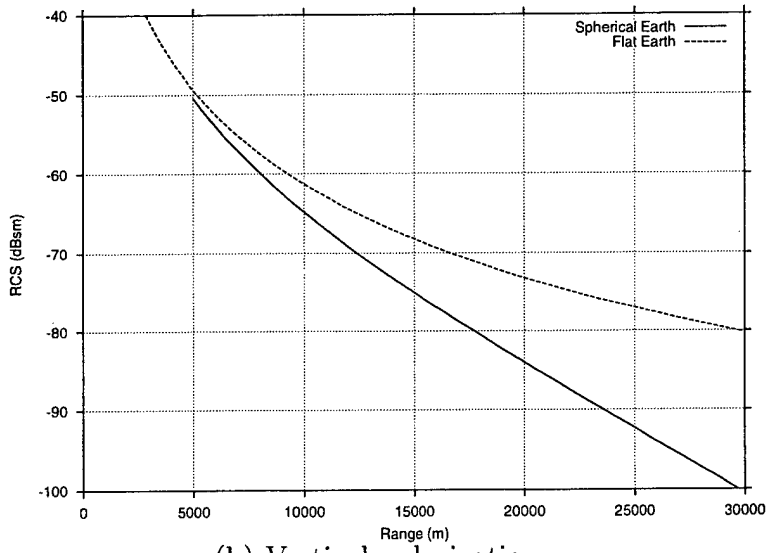

(b) Vertical polarization.

Figure 4.8: RCS vs. range for a block target on a spherical and flat earth. Frequency = 1 GHz, $\phi = 0°$, transmitter height = 10 m, horizon at 13 km.

Chapter 5

Conclusions and Summary of Recommended Approach

5.1 Conclusions of Third Year Study

Chapter 2 presented the results of a more thorough statistical analysis of the scattering from a 2D target on an ocean surface, including vertical polarization which hadn't been included before. The results again verified that the RCS tends to become more coherent as the incident field becomes coherent, i.e., for low wind speeds or low elevation angles. The coherent RCS was compared with the RCS computed with the coherent component of the incident field, and was shown to be different unless the incident field is highly coherent. The coherent incident field approach is therefore not recommended, also because the coherent incident field does not satisfy the boundary condition at the sea surface.

The RCS of some simple 3D targets on rough ocean surfaces was studied in Chapter 3. For the horizontal co-polarization case, the same characteristics of the RCS patterns was observed as in 2D, i.e., the RCS tends to be more coherent when the incident field is coherent and the rough surface RCS tends to converge to the flat surface RCS for low elevation angles. However, the vertical co-pol case showed some unexpected results near the Brewster angle. The rough surface RCS patterns converged for low elevation angles, but they did not converge to the flat surface case. It is still not clear if this is a real effect or a numerical artifact because an independent reference solution is not available for validation. The IPO code was checked

against a rigorous method of moments code for a rough PEC sea surface, and was checked against the infinite flat impedance surface case. However, a solution for a rough impedance surface with a PEC target is not currently available. The results will be checked when this solution or experimental validation becomes available. If the effect is physical, it probably has something to do how the rough surface affects the plane wave reflection near the Brewster angle.

A small scale Monte Carlo simulation was performed for 3D targets in Chapter 3. Again it was shown that the coherent RCS may be considerably different than the RCS computed with the coherent component of the incident field. It was also shown that the average and peak RCS levels for a target on a rough surface can be considerably higher than the same target on a flat surface. The tilted plane model was tested in this chapter for 3D targets via the roll angle plot. Rolling the target in the plane of incidence gave a good indication of the amount of variation in the co-polarized RCS, and the amount of roll was related to the average slope of the long ocean waves. However, it did not predict the cross-polarization introduced by the rough surface. It is possible that rolling the target in other planes than the plane of incidence may give a better indication of the cross-pol component.

The incident field and scattering from a 3D target on a spherical earth was studied in Chapter 4. The vertical polarization case was included for the first time in this study for both the PWE results and the Fock Airy function solution. A ray-optical model for the incident field was described. It was observed that for very rough surfaces the coherent scattering coefficient may over-predict the coherent component of the incident field. This bears further investigation. As expected, the RCS plots for a target on a spherical earth as a function of range showed how a spherical earth can greatly reduce the RCS compared with a flat earth, especially as the target moves beyond the horizon. The V-pol RCS was about 4 dB lower than H-pol for the target considered.

5.2 General Observations

The study of the radar scattering from targets on a rough sea surface has revealed some interesting observations, some expected and some not. It has been observed in both 2D and 3D that the RCS of the target becomes more coherent as the incident field becomes more coherent. However, as was shown during the second year study in the 2D RCS vs. time results, there are still some variations in the RCS even for low grazing angles where the incident field is highly coherent. This is explained using the tilted plane model, similar to the "two-scale" or composite model of ocean scattering [4, 20, 21]. It was shown that the slow variations in the RCS could be correlated with the movement of the target up and down on the long waves. The roll angle plots for a target on a flat surface were shown to predict as much or more variation in the RCS than that caused by the rough surface.

The 3D results indicate that the rough surface introduces a significant cross-polarization component to the RCS. The roll angle plot does not predict the cross-pol when the target is rolled in the plane of incidence. Rolling the target in other planes may give a better indication of the cross-pol effect, but this is left to a future investigation. Also left to future investigation is the effect of a directional rough surface wherein the long waves propagate in the direction of the wind. This would directly impact the tilted plane model because the rolling would be in the plane of the long waves.

Some unexpected results were observed for vertical polarization in 3D near the Brewster angle. The RCS patterns for a target on rough sea surfaces tended to converge for low elevation angles, but did not converge to the flat surface pattern. The reason for this is currently not explainable here, but may become resolved in the future when independent validations become available.

Finally, it has been apparent throughout that the numerical models of the target and sea surface are limited by existing computational resources, and it is not practical to apply these models to realistically sized 3D ships at radar frequencies. They have only been used to study the phenomenology in order to obtain enough understanding to develop more appropriate methods. The RCS vs. roll angle plot for a target on a flat surface is still considered by the

investigators to be the best tool for predicting the variations of the RCS due to a rough sea surface, because a realistic target will roll with the waves and the local sea surface in the vicinity of the target tends to look like a tilted plane. In the tilted plane model the incident field is ray-optical and the flat surface (or spherical earth) Green's function may be used to compute the RCS via existing codes. The RCS vs. elevation and azimuth angle plots are also important for understanding the variation of the RCS. The next section summarizes the recommended approach.

Approaches which include a deterministic rough sea surface in the model are still intractable. As was shown during the first year of this study, even if the incident field is represented accurately, the scattering from the target must also be found in the presence of the rough surface. If a locally planar approximation for the surface is used to find the scattered field, then the incident and scattered fields will not satisfy the same boundary condition and a non-physical scattering mechanism may be introduced. It is possible that high-frequency ray methods could be applied by finding the multiple reflection paths of rays from the surface to the target. But such an approach would be highly computationally intensive because of the huge number of rays involved. It is also not appropriate for low grazing angles because the waves will cast shadows on the target which introduce non-physical scattering mechanisms. It is possible that these obstacles will be overcome in future developments.

5.3 Prescription for Computing RCS of Marine Targets

In this section the recommended ray-optical approach for predicting the scattering from a realistically large target on the sea surface is outlined. This approach is meant for practical problems when rigorous numerical approaches are not tractable. Figure 4.1 depicts the ray-optical characterization of the incident field illuminating the target on a spherical earth, and is repeated here in Figure 5.1. In the following, S refers to the surface which encapsulates the portion of the target above the water line.

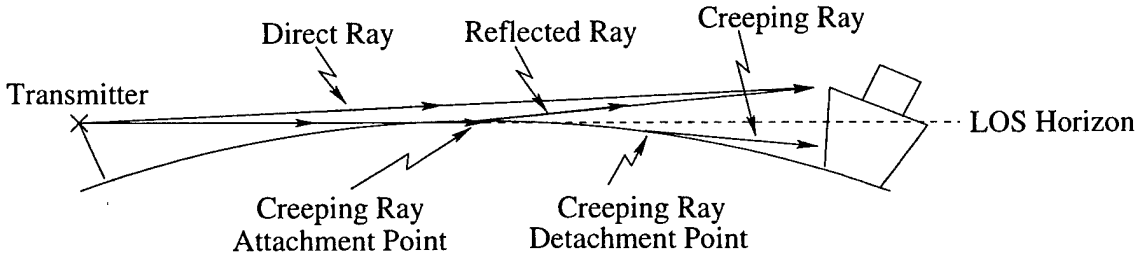

Figure 5.1: Ray-optical model for the incident fields illuminating a target on a spherical earth.

Recipe for Ship RCS Computations

1. Find the ray-optical representation of the incident electric and magnetic fields $\bar{E}^i, \bar{H}^i$ over S due to a unit-amplitude horizontal or vertical dipole transmitting source located over a smooth spherical earth sea surface. Use the Fock Airy function solution for the creeping ray [15, 16] and the geometrical optics solution for the incident and reflected rays [5]. The sea water may modeled with an equivalent surface impedance as given by Eq. (3.1). The EREPS code could also possibly be adapted for this step [22].

2. Find the scattered fields $\bar{E}^s, \bar{H}^s$ over S due to the incident field found in Step 1. This is done by assuming the target is on an infinite flat sea surface and using the Sommerfeld half-space Green's function. Existing RCS codes may be easily modified for this task [23].

3. Find the co-polarized backscattered field at the transmitter location (T) using the reciprocity integral:

$$E_c^s(T) = \int_S \left(\bar{E}^s \times \bar{H}^i - \bar{E}^i \times \bar{H}^s\right) \cdot \hat{n} dS \tag{5.1}$$

   where $\hat{n}$ is the outward-pointing unit normal vector for the surface S. A more detailed development of the reciprocity integral may be found in [1].

4. Repeat Steps 1-3 as a function of the target rotation angle (azimuth) and roll angle. It is advisable to roll the target in the plane of incidence and the orthogonal plane.

5.4 Suggested Future Work

There remains to investigate some issues which were not resolved during the course of this study. It has been observed from the numerical simulations that the analytic coherent scattering coefficient of (2.4) may over-predict the coherent component of the sea scattered field for low grazing angles when the surface is very rough. Further numerical and experimental validation is necessary. Further validation is also necessary to resolve the discrepancy between the V-pol and H-pol RCS near the Brewster angle. The V-pol case did not show the expected convergence to the flat surface case for low elevation angles near the Brewster angle.

It was planned to investigate the effect of a directional rough surface where the long waves propagate in the direction of the wind. Unfortunately, a model for a directional ocean wave spectrum is not currently well-developed, and time did not permit a meaningful investigation. Such an ocean spectrum would give a directional property to the long waves, but the small scale waves would remain omni-directional.

Another interesting application of the numerical models used in this study would be to investigate the effect of the rough sea surface on the radar image of a target. This would be relatively easy to implement using the existing computer codes developed under this study.

Finally, as mentioned earlier, it is still of interest to develop ray methods that can include the rough sea surface in the computation of the RCS of a surface target. For higher frequency bands, such as used by aircraft and missile radars, the incident field may not be coherent even for low grazing angles. Then it would be of interest to ray-optically predict the propagation of the incident field over a deterministic rough ocean surface. The rays that illuminate the ship could then be used to find the RCS directly. However, this is not an easy task because the long waves will cast ray shadows, and if diffraction (via edge, creeping, or surface waves) is not included, the shadow boundaries will introduce non-physical scattering mechanisms. Furthermore, such an approach would be very computationally intensive because a tremendously large number of rays would have to be traced over may wave crests from the transmitter to the target.

Bibliography

[1] R.J. Burkholder, M.R. Pino, and D.-H. Kwon, "Development of Ray-Optical Methods for Studying the RCS of 2D Targets on a Rough Sea Surface," The Ohio State University ElectroScience Laboratory Technical Report 735231-1, January 1999.

[2] R.J. Burkholder, D. Colak, and H. Kiper, "Numerical Investigation of the RCS of 3D Targets on a Rough Sea Surface," The Ohio State University ElectroScience Laboratory Technical Report 735231-2, January 2000.

[3] L. Tsang, J. A. Kong, and R. T. Shin, *Theory of Microwave Remote Sensing.* Wiley, New York, 1985.

[4] M. Skolnik, *Radar Handbook.* McGraw-Hill, New York, 1990.

[5] P. H. Pathak, *Antenna Handbook, Theory Application and Design: Techniques for High Frequency Problems.* Van Nostrand Reinhold, 1988.

[6] R. F. Harrington, *Time-Harmonic Electromagnetic Fields.* McGraw-Hill, New York, 1961.

[7] D. Torrungrueng and E. H. Newman, "The Multiple Sweep Method of Moments (MSMM) Analysis of Electrically Large Bodies," *IEEE Trans. Ant. Prop.*, vol. 45, pp. 1252–1258, Aug. 1997.

[8] D. Çolak, and E.H. Newman, "The Multiple Sweep Method of Moments (MSMM) design of wide-band antennas," *IEEE Trans. on Antennas and Propagat.*, vol. 46, pp. 1365-1371, Sept. 1998.

[9] M.R. Pino, L. Landesa, J.L. Rodríguez, F. Obelleiro, and R.J. Burkholder, "The Generalized Forward-Backward Method for Analyzing the Scattering from Targets on Ocean–Like Rough Surfaces," *IEEE Trans. Antennas and Propagation*, Vol. 47, No. 6, pp. 961-969, June 1999.

[10] M.R. Pino and F. Obelleiro, and R.J. Burkholder, "Spectral Acceleration of the Generalized Forward-Backward Method," submitted to *IEEE Trans. on Antennas and Propagation*, July 1999.

[11] W. J. Pierson and L. Moskowitz, "A proposed spectral form for fully developed wind seas based on the similarity theory of S.A. Kitaigorodskii," *J. Geophys. Res.*, vol. 69, pp. 5181–5190, 1964.

[12] R.J. Burkholder, M.R. Pino, and F. Obelleiro, "A Monte Carlo Study of the Rough Sea Surface Influence on the Radar Scattering from 2D Ships," To appear in *IEEE Antennas and Propagation Magazine.*

[13] F. Obelleiro, J.L. Rodriguez, and R.J. Burkholder, "An Iterative Physical Optics Approach for Analyzing the Electromagnetic Scattering by Large Open-Ended Cavities," (co-authors F. Obelleiro and J.L. Rodriguez), *IEEE Transactions on Antennas and Propagation,* Vol. 43, No. 4, pp. 356-361, April 1995.

[14] R.J. Burkholder, "A Forward-Backward Iterative Physical Optics Algorithm for Cavity Scattering Problems," USNC/URSI Radio Science Meeting, p. 224, Orlando, Florida, July 11-16, 1999.

[15] V.A. Fock, Electromagnetic Diffraction and Propagation Problems, Pergamon Press Ltd., New York, 1965.

[16] M.L. Meeks, Radar Propagation at Low Altitudes, Artech House, Inc., Dedham, MA, 1982.

[17] A.E. Barrios, "Parabolic Equation Modeling in Horizontally Inhomogeneous Environments," *IEEE Trans. Antennas Propagat.,* Vol. 40, No. 7, p. 791, July 1992.

[18] A.E. Barrios, "A Terrain Parabolic Equation Model for Propagation in the Troposphere," *IEEE Trans. Antennas Propagat.*, Vol. 42, No. 1, p. 90, Jan. 1994.

[19] D.R. Sailors, A.E. Barrios, W.L. Patterson, and H.V. Hitney, "Advanced Propagation Model (APM) Computer Software Configuration Item (CSCI) Documents," Technical Document 3033, Space and Naval Warfare Systems Center, San Diego, CA, August 1998.

[20] J.W. Wright, "A new model for sea clutter," *IEEE Trans. Ant. Prop.,* Vol. 16, pp. 217-223, 1968.

[21] G.R. Valenzuela, "Theories for the interaction of electromagnetic and oceanic waves: a review," *Bound. Layer Meteorology,* Vol. 13, pp. 61-85, 1978.

[22] W.L. Patterson, C.P. Hattan, H.V. Hitney, R.A. Paulus, A.E. Barrios, G.E. Lindem, K.D. Anderson, "Engineer's Refractive Effects Prediction System (EREPS) Revision 2.0," Technical Document 1342, Naval Ocean Systems Center, San Diego, CA, February 1990.

[23] R.J. Marhefka, "Radar Cross Section - Basic Scattering Code RCS-BSC (Version 2.0) User's Manual," The Ohio State University ElectroScience Laboratory Technical Report 718295-15, February 1990.